ROYAL SOCIETY OF CHEMISTRY

REVIEW ARTICLE

Check for updates

Harnessing single-atom catalysts for CO_2 electroreduction: a review of recent advances

Chang Chen,†[a] Jiazhan Li,†[c] Xin Tan,†[a] Yu Zhang,[a] Yifan Li,[d] Chang He,[a] Zhiyuan Xu,[a] Chao Zhang*[b] and Chen Chen [ID] *[a]

Electrochemical CO_2 reduction is an effective pathway to convert CO_2 into valuable fuels and chemicals, which provides a potential alternative to fossil fuel resources and plays a notable role in mitigating environmental issues and energy crises. The feasibility of the CO_2 reduction reaction (CO_2RR) hinges on the development of catalysts that feature high activity, selectivity, and stability. As a new research frontier, single-atom catalysts (SACs) have shown immense potential in the field of CO_2 reduction by virtue of their unique geometric/electronic structures, and have also provided new opportunities for atomic-level understanding of structure–function relationships. Therefore, this review aims to outline recent advances of SACs for CO_2RR. We start by introducing the current research status and general synthesis strategies of SACs, and then shift our focus to analyzing the various regulation strategies and deciphering the structure–function relationships of SACs in the CO_2RR. Finally, we propose future directions and opportunities for CO_2RR-oriented SACs, while also highlighting potential challenges that may be encountered along the way.

Broader context

Excessive emission of CO_2, which causes environmental degradation and energy crises, has caused panic in the scientific community and the general population. Therefore, the development of effective CO_2 conversion and utilization technologies is urgent and of great significance. One promising approach is the use of clean energy to drive electrochemical CO_2 reduction, which can help mitigate the negative effects of CO_2 and generate high-value-added products. However, the extreme inertness of linear CO_2 molecules and the competing hydrogen evolution reaction severely affect their catalytic activity and selectivity. Fortunately, single-atom catalysts (SACs), with their unique geometric/electronic structures, have emerged as a frontier research area for the CO_2 reduction reaction (CO_2RR) and have achieved significant progress. To accelerate the research progress of SACs in the CO_2RR, it is necessary to summarize and review the current state of this field and provide guidance for future research. This article first introduces the basic parameters of the CO_2RR and summarizes the mainstream reaction mechanisms for generating C_1 and C_2 products. Then, the current development status of SACs is outlined, along with common synthesis strategies. The application of SACs in the CO_2RR is then highlighted, including analyzing the various regulation strategies and deciphering the structure–function relationships of SACs in the CO_2RR. Finally, future potential directions and challenges confronted by SACs in the realm of the CO_2RR are also contemplated.

[a] Engineering Research Center of Advanced Rare Earth Materials, Department of Chemistry, Tsinghua University, Beijing 100084, China.
E-mail: cchen@mail.tsinghua.edu.cn

[b] MOE International Joint Laboratory of Materials Microstructure, Institute for New Energy Materials and Low-Carbon Technologies, School of Materials Science and Engineering, Tianjin University of Technology, Tianjin 300384, China.
E-mail: czhang@email.tjut.edu.cn

[c] State Key Laboratory of Chemical Resource Engineering, College of Chemistry, Beijing University of Chemical Technology, Beijing 100029, China

[d] Department of Chemical and Materials Engineering, University of Alberta, Edmonton, AB, T6G1H9, Canada

† Chang Chen, Jiazhan Li, and Xin Tan contributed equally to this work.

1. Introduction

The continuous consumption of fossil fuels has led to excessive emission of CO_2 into the Earth's atmosphere, which has consequently caused climate change and environmental crises, and provoked great concern in the scientific community and the general population.[1–5] Besides, as CO_2 accounts for over 96% of the Martian atmosphere, utilizing CO_2 resources for Mars exploration is also a new research direction for future human space programs.[6] Thus, effective CO_2 conversion and utilization technologies are pressing and important grand research challenges in maintaining carbon neutrality balance and alleviating energy shortages. To address the CO_2 issue, different routes have been proposed: (1) capturing and storing

CO_2;[3,7-9] (2) improving the efficiency of fossil fuel combustion and reducing emissions;[10] and (3) chemically converting CO_2 to form high-value-added products.[11-16] Among these options, the electrochemical CO_2 reduction reaction (CO_2RR) has emerged as one of the most promising routes to addressing the issues of recycling CO_2 and producing valuable chemical products.[17-20] Furthermore, the CO_2RR can be driven by renewable (but intermittent) energy sources (such as wind, solar, and tidal) without extra CO_2 emission, and the reduction process can be easily performed by adjusting the potential range and current densities under ambient pressure and temperature.[17,21,22]

However, the CO_2RR suffers from two stable C=O double bonds (bond energy, 806 kJ mol^{-1}) in the extremely inert linear CO_2 molecule, generally leading to a low energy efficiency with high overpotentials.[23,24] Table 1 summarizes the standard potentials E^0 (with respect to the standard hydrogen electrode, SHE) of CO_2RR processes and the competitive hydrogen evolution reaction (HER) in aqueous media.[17,18,25] Specifically, a significant external driving force is needed to initiate the single-electron reduction of CO_2 to the key intermediate $*CO_2^-$ during the CO_2RR process ($CO_2 + e^- \rightarrow *CO_2^-$), or to undergo the proton-coupled electron transfer (PCET) process and produce different hydrocarbons and oxygenates, including (but not limited to) CO, HCOOH, HCHO, CH_3OH, CH_4, C_2H_4, and C_2H_5OH.[26,27] In addition, thermodynamically, the reduction potentials for the main reduction products mentioned above in the CO_2RR typically fall within the range of ± 0.2 V from that of the HER.[17] However, the presence of a high barrier for CO_2 activation and the involvement of multiple electron transfer steps in the reaction pathways of the CO_2RR result in sluggish kinetics and side reactions involving the HER. As a result, the CO_2RR usually shows high overpotentials and poor selectivity. In this regard, developing efficient and highly selective electrocatalysts to promote CO_2RR technology towards industrial applications is the key to addressing the aforementioned challenges.[20,24]

During the past decades, a broad class of electrocatalysts has been developed for the CO_2RR, including metals,[28-31] metal oxides,[32-37] metal alloys,[38-41] molecular compounds,[42] metal phosphides/chalcogenides,[43,44] and metal-free carbon-based materials.[45-47] Most notably, single-atom catalysts (SACs) have emerged as a new family of catalytic materials by virtue of their distinctive structural properties and exceptional catalytic performances.[48,49] As a new class of frontier materials, the SACs feature maximized atomic utilization with their active sites isolated with each other but interacting with the support.[50] In 2011, Qiao et al. reported a single-atom platinum catalyst supported on iron oxide nanocrystallites (Pt_1/FeO_x), and the concept of a "single-atom" catalyst was proposed for the first time.[51] Since then, the concept was quickly accepted by the scientific community and the scope of relevant materials has broadened significantly. Various materials have been explored as the support (such as carbon materials,[52,53] MXenes,[54] oxides,[55] and carbides[56]), and the elements for the metal active centers have nearly covered all the non-radioactive metals in the periodic table.[57,58] The CO_2RR over SACs can be traced back to the 1970s, when molecular catalysts (cobalt/nickel phthalocyanines) were used as the active sites.[59] With the development of synthesis technology, characterization technology (high-angle annular dark-field scanning transmission electron microscopy (AC-HAADF-STEM) and X-ray absorption spectroscopy (XAS), in particular), and theoretical computational chemistry, the establishment of the structure–function relationship between the structure of SACs and the performance of the CO_2RR has made great progress. Specifically, SACs have adjustable coordination environments and structures, making it easier to obtain uniform catalytic active centers. Furthermore, SACs can also serve as an ideal bridge between homogeneous and heterogeneous catalysis.[48-50] For the CO_2RR, the reaction process typically involves multiple PCET steps accompanied by complex intermediates, and SACs with well-defined structures have become an ideal research model. This could help to identify the reaction mechanism and to understand the structure–function relationship of SACs in the CO_2RR, guiding us to develop new advanced electrocatalysts. For example, SACs featuring Ag, Mn, Fe, and Ni single-atom active sites often exhibit excellent CO selectivities.[27] In the process of the rational design of CO_2RR catalysts, researchers have found that the generation of non-CO products (such as C_{2+} products) is very difficult and complex.[60] Because of the isolation and simplicity of their active sites, SACs are not so competent in some cases, prompting researchers to develop dual-atom catalysts or multi-atom catalysts (DACs or MACs) with more than one type of active sites.[61,62] There could be a synergistic effect between the dual-atom sites or multi-atom sites, providing more possibilities and pathways for the generation of high value-added products.[63-67]

Compared with other types of heterogeneous catalysts, SACs have unique advantages in geometric/electronic structures, which gives them great potential to become marvellous catalysts for the CO_2RR. In this review, as shown in Fig. 1, we use the metaphor of an alchemical furnace as the main concept, with three supporting pillars representing the general synthesis strategies for SACs. The four different "elixirs" within the furnace chamber represent the diverse regulation strategies for SACs in CO_2RR applications. Eventually, the reactant CO_2 undergoes transformations within this alchemical furnace to produce various products. At the end of this review, we present an outlook on the future directions, opportunities, and challenges in the field of SACs for the CO_2RR.

Table 1 Standard potentials (V vs. SHE) of the CO_2RR in aqueous media at 1 atm and 25 °C

| Half-cell reaction	Standard potentials
$2H^+ + 2e^- \rightarrow H_2$	−0.42
$CO_2 + e^- \rightarrow *CO_2^-$	−1.9
$CO_2 + 2H^+ + 2e^- \rightarrow CO + H_2O$	−0.52
$CO_2 + 2H^+ + 2e^- \rightarrow HCOOH$	−0.61
$CO_2 + 4H^+ + 4e^- \rightarrow HCHO + H_2O$	−0.51
$CO_2 + 6H^+ + 6e^- \rightarrow CH_3OH + H_2O$	−0.38
$CO_2 + 8H^+ + 8e^- \rightarrow CH_4 + 2H_2O$	−0.24
$2CO_2 + 12H^+ + 12e^- \rightarrow C_2H_4 + 4H_2O$	−0.34
$2CO_2 + 12H^+ + 12e^- \rightarrow C_2H_5OH + 3H_2O$	−0.33
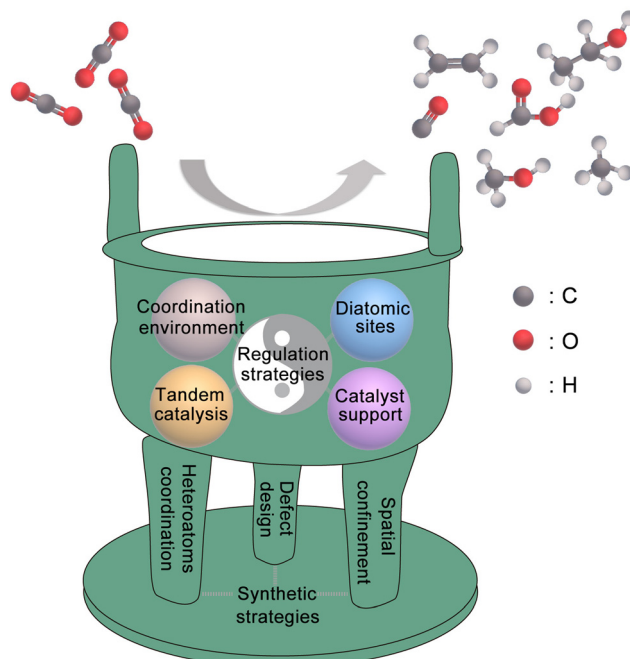
Fig. 1 Schematic diagram of the SACs for the CO_2RR in this review (including the general synthesis strategies for SACs and the regulation strategies of SACs for the CO_2RR).

2. Fundamental parameters and reaction mechanisms of the CO_2RR

2.1 Fundamental parameters of the CO_2RR

It is necessary to introduce the fundamental parameters before proceeding further with this review. At present, the standard metrics used to evaluate and compare the performance of CO_2RR electrocatalytic materials mainly include the following: faradaic efficiency (FE), onset potential, current density, partial current density, stability, turnover frequency (TOF).[25,68]

2.1.1 Faradaic efficiency. FE refers to the percentage of the number of electrons consumed in the generation of the target product to the total number of electrons consumed, which can be calculated using the following formula: FE = $\alpha nF/Q$. Among them, α is the number of electron transfers that generate a specific product (for example, if CO_2 is reduced to carbon monoxide (CO), the number of electrons transferred in this process is 2, α = 2); n is the total amount of a specific product (in moles); F is the Faraday constant (96 485 C mol^{-1}); Q represents the total amount of charge during the CO_2RR process. By analysing the FE, the difference in selectivity of different catalysts for the CO_2RR can be directly compared.

2.1.2 Onset potential. Thermodynamically, CO_2RR is a non-spontaneous process. The onset potential is the lowest externally applied potential that can initiate the CO_2RR (with the generated target product detectable). Since there is a certain potential barrier to overcome in the process of the CO_2RR, the onset potential is generally more negative than the standard reduction potential. Overpotential is the difference between the thermodynamic standard potential and the external potential

of a specific CO_2RR, typically used to activate inert CO_2 molecules to form $^{\star}CO_2^{-}$ anionic radicals, driving material exchange and electron transfer in the CO_2RR process. The onset potential is the parameter that can directly indicate the magnitude of the overpotential and assess the catalytic activity of the electrocatalyst.

2.1.3 Current density. Current density refers to the current passing through a unit electrode area, which is the ratio of the current magnitude to the electrochemical active area, and can be used to estimate the reaction rate. The magnitude of current density is one of the indicators of whether a catalytic system can be commercialized.

2.1.4 Partial current density. Partial current density expresses the effective current density that drives the formation of a specific product, which can be obtained by multiplying the FE for that specific product by the total current density. Commonly, the partial current density is not only dependent on the activity of the electrocatalyst itself, but also influenced by experimental conditions (electrodes, cell components, electrolyte, etc.). For example, the H-type cell configuration is limited by the solubility and diffusion of CO_2 in the aqueous electrolyte, whereas the flow cell configuration is equipped with gas diffusion electrode components (which can continuously provide CO_2 gas and electrolyte), thus achieving high current density.[69]

2.1.5 Stability. Stability is an important metric that indicates whether a catalyst can be commercially applied. Therefore, stability is no less important for a catalyst than its activity and selectivity. At present, the stability tests of catalysts in the laboratory usually take only a few dozen hours, which is far from enough for the commercialization of catalysts. The decline of stability is usually caused by the coupling of the deactivation of the catalytic active site, the destruction of the catalyst structure, and the continuous consumption of electrolytes. An ideal CO_2RR catalyst should be designed to retain both current density and FE without increasing the overpotential during long-term continuous operation.

2.1.6 Turnover frequency. For decades, TOF has been an accurate descriptor for the intrinsic activity of catalysts. While current density is important in determining the apparent activity, but it is affected by parasitic reactions centered on the catalyst and competitive reactions centered on the electrolyte. Fortunately, TOF provides a precise measure of the intrinsic activity without involving these electrocatalytic phenomena. TOF refers to the quantity of target products produced on one active site in unit time, and its calculation formula is as follows: TOF = [product (mol)]/[active sites (mol)]/time. Among these, there are multiple analytical methods available to quantify reactants or products; however, determining the exact number of active sites is often the most challenging task. In particular, for cluster/nanoparticle catalysts, even when the active sites are identified, each site may have a different chemical environment. In contrast, for SACs, the situation is much simpler. Currently, it is presumed that the active sites in SACs are isolated, and their chemical environments are almost uniform. Hence, it can be assumed that each individual metal atom acts as an active site.[25]

2.2 Reaction mechanisms of the CO$_2$RR

The CO$_2$RR is a rather complex process involving multiple PCET steps, with different reaction pathways associated with 2–18 electron transfers, resulting in a wide distribution of products, including C$_1$ products (such as CO, HCOOH, CH$_3$OH, HCHO, and CH$_4$), and C$_{2+}$ products (such as C$_2$H$_4$, C$_2$H$_5$OH, CH$_3$COOH, and CH$_3$COCH$_3$). Great efforts have been made both experimentally and theoretically to elucidate the CO$_2$RR mechanism, but there is still a lack of consensus on some reaction steps, and their reaction mechanisms are still not fully understood. More *in situ* characterization techniques, even more advanced coupled multi *in situ* characterization techniques, as well as theoretical calculations are needed to further decipher the CO$_2$RR reaction mechanism. Here, we summarize the possible reaction pathways of C$_1$ products and the main C$_2$ products based on the current prevailing understanding of CO$_2$RR mechanisms, so as to design high-activity, high-selectivity, and high-stability SAC catalysts rationally.

2.2.1 **Pathways for C$_1$ products.** CO is the most common product of the CO$_2$RR, and a large portion of SACs (such as Fe, Co, Ni, and Mn) exhibit high CO selectivity (Fig. 2).[70] Although researchers have made significant efforts to analyze the pathways of CO generation, a clear picture of the reaction mechanism remains controversial. At present, the reaction pathway from CO$_2$ to CO through *COOH intermediates is widely acknowledged, which can be achieved through a PCET process or proton transfer process after a preferential electron transfer process (Fig. 3).[70–74] The resulting *COOH intermediate would undergo the next PCET process to convert into *CO, and the weakly bound *CO would eventually desorb from the catalyst surface to produce CO. In the generation process of other C$_1$ products (such as HCHO, CH$_3$OH, and CH$_4$), *CO is widely considered to play a crucial role as an intermediate.[70] Peterson *et al.* demonstrated that the most favorable thermodynamic pathway for the CO$_2$RR on the Cu(211) surface is the formation of *CO and subsequent hydrogenation to generate *HCO, *H$_2$CO, and *H$_3$CO.[75] Among them, *H$_2$CO can selectively desorb to form HCHO or form *H$_3$CO, and the *H$_3$CO can further form CH$_3$OH through the PCET process. Nie *et al.* proposed a plausible pathway for generating CH$_4$ on the basis of theoretical analysis: *CO is considered to generate the *COH intermediate, which is further reduced to adsorbed *C, and sequentially reduced to generate *CH, *CH$_2$, *CH$_3$, and the final product CH$_4$.[76]

Unlike other C$_1$ products, the generation of HCOOH or HCOO$^-$ has a reaction pathway of its own. The generation of HCOOH or HCOO$^-$ may be achieved through an intermediate, which is believed to be mainly through the binding of oxygen atoms to the catalyst surface, and the generation of this intermediate may have two different pathways: (1) CO$_2^-$ radicals bind to the catalyst surface and react with adjacent water molecules or protons to generate HCOO$^-$ or HCOOH; (2) CO$_2$ is directly inserted into metal–hydrogen or metal–hydroxyl bonds to form intermediates, which further yields HCOOH or HCOO$^-$.[70,77]

2.2.2 **Pathways for C$_2$ products.** The reaction mechanisms of C$_2$ products are even more complex. Here we summarize the plausible reaction mechanisms of the two main C$_2$ products: C$_2$H$_4$ and C$_2$H$_5$OH (Fig. 3). *CO is considered a key intermediate for the formation of C$_2$ products. It can directly form the *C$_2$HO$_2$ intermediate through symmetric dimerization followed by further hydrogenation. Alternatively, it can first undergo hydrogenation to produce *CHO or *COH, which then asymmetrically couple with *CO to yield the *C$_2$HO$_2$ intermediate.[13,71,78] Among the various catalysts developed so far, Cu-based catalysts are the only ones widely recognized capable of catalyzing the CO$_2$RR to C$_{2+}$ products because of their moderate binding energy with *CO.[79,80] After the C–C coupling, multiple PCET steps ensue to obtain the key *C$_2$H$_3$O intermediate that determines the formation of C$_2$H$_4$ and C$_2$H$_5$OH products. However, in most catalyst systems, the selectivity for C$_2$H$_4$ is higher than that for C$_2$H$_5$OH because the energy barrier from the *C$_2$H$_3$O intermediate to the C$_2$H$_4$ product is lower than to the C$_2$H$_5$OH product.[81] Although Cu is considered to have unique advantages in the selectivity of C$_{2+}$ products, there are few reports on Cu SACs for producing C$_{2+}$ products, as it is difficult to promote C–C coupling or *CO dimerization on isolated Cu single atoms. Thus, in the future, more modifications on Cu-based catalysts will be considered to construct more homonuclear or heteronuclear active sites, in order to expand the range of C$_{2+}$ products and to improve their selectivity.[82–84]

3. Synthesis strategies and characterization techniques of SACs

3.1 Synthesis strategies of SACs

The term "SACs" was coined on the basis of the characteristics of their active centers; however, in reality, individual atoms
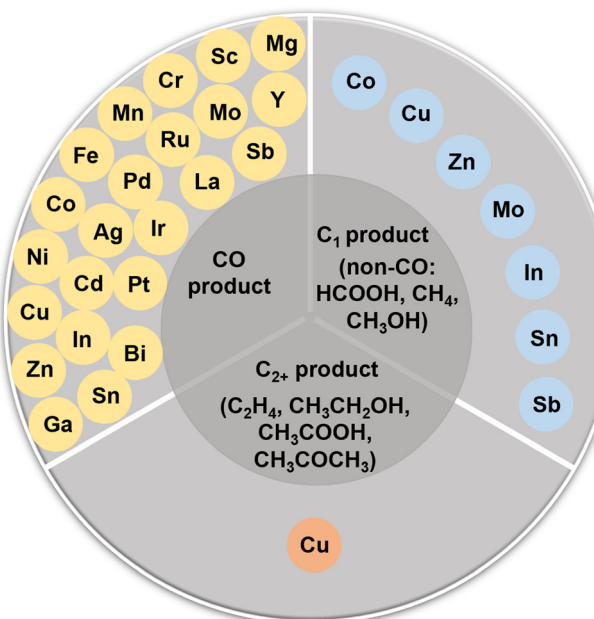

Fig. 2 Schematic diagram of the reported elements in SACs for CO$_2$RR.
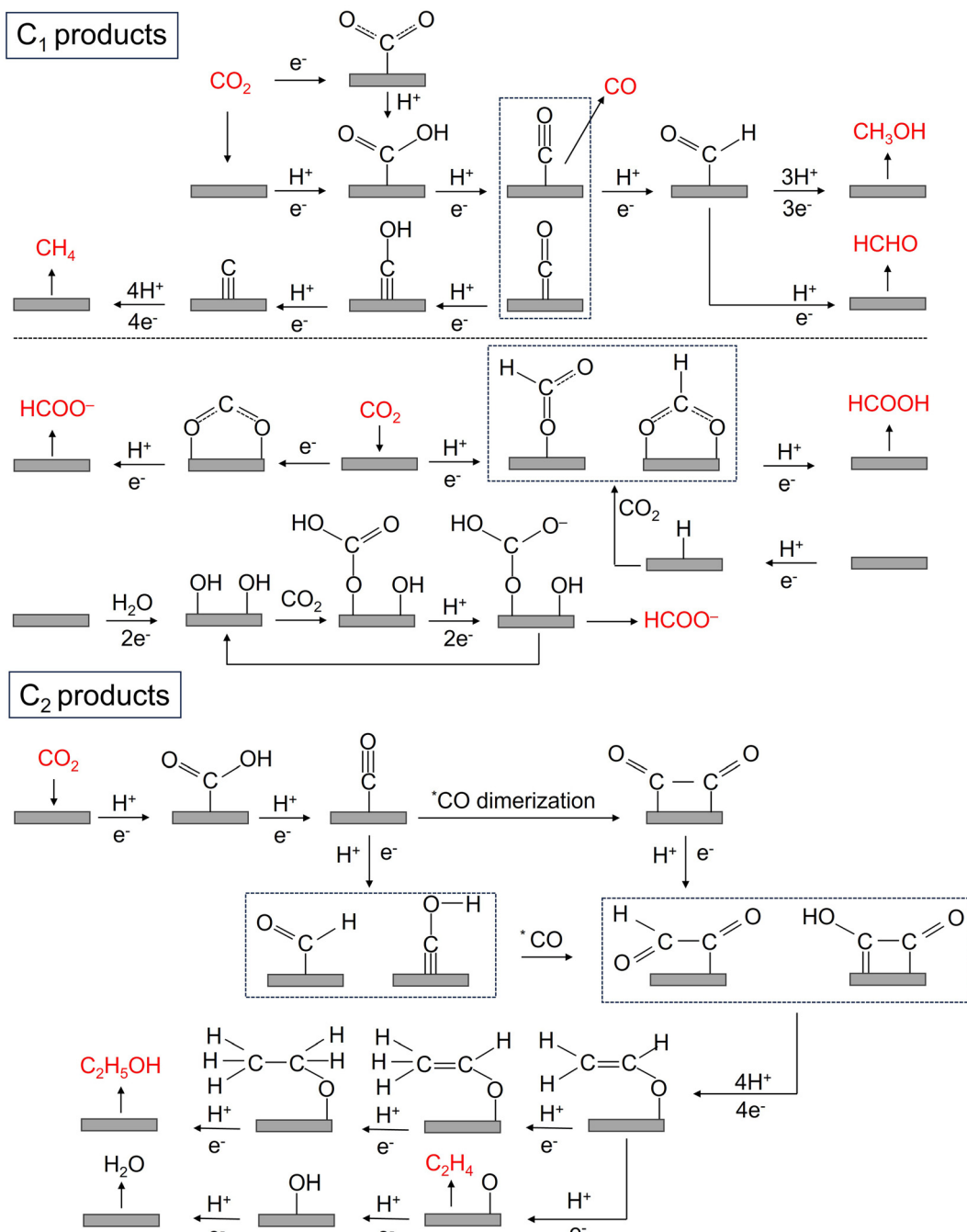
Fig. 3 The possible reaction pathways of C_1 and C_2 products in the CO_2RR.

cannot exist in isolation but instead rely on a supporting material.[48,49] Owing to their high surface energy, isolated metal atoms have a tendency to aggregate into thermodynamically more stable metal clusters. Hence, the interaction between the support and single atoms is crucial in preventing the aggregation of individual atoms. Since the concept of "single-atom-catalysts" emerged in 2011,[51] various strategies have been proposed to synthesize SACs with high metal loadings and high CO_2RR performances. In this section, we mainly discuss the challenges and current strategies for increasing the metal loading and tuning the electronic structure of SACs, which are categorized into "heteroatom coordination strategy", "spatial confinement strategy" and "defect design strategy". In addition, some other advanced synthesis strategies of SACs are also introduced.

3.1.1 Heteroatom coordination strategy. The rational design of coordination sites with the aim of adsorbing and binding metal precursors or metal atoms to prevent their agglomeration and migration has been a basic design principle for the synthesis of SACs. Owing to the strong interaction

between metal atoms and coordinating atoms, metal single atoms can be uniformly and firmly anchored onto the supports. The construction of highly active and stable SACs using the coordination strategy requires the selection of suitable reactants (*e.g.*, metal precursors and coordination polymorphs) and appropriate experimental conditions. Several non-metallic elements with lone pairs of electrons are good coordination sites because of their affinity for metals, such as N, O and S.[20,21,48,85]

Many studies have already shown that the physicochemical state of SACs can be optimized by adjusting the coordination number, coordination structure and coordination environment of the metal single-atom centers, thus further improving their CO$_2$RR performance. The coordination number of the central metal atoms can modulate the electronic structure of the catalyst and thus alter the catalytic performance. Wang *et al.* reported two Co-based catalysts with different coordination numbers, denoted as Co–N$_4$ and Co–N$_2$. The catalysts were prepared by adjusting the pyrolysis temperature to control the extent of volatilization (Fig. 4a).[86] Zhang *et al.* devised a post-synthetic metal substitution (PSMS) strategy in combination
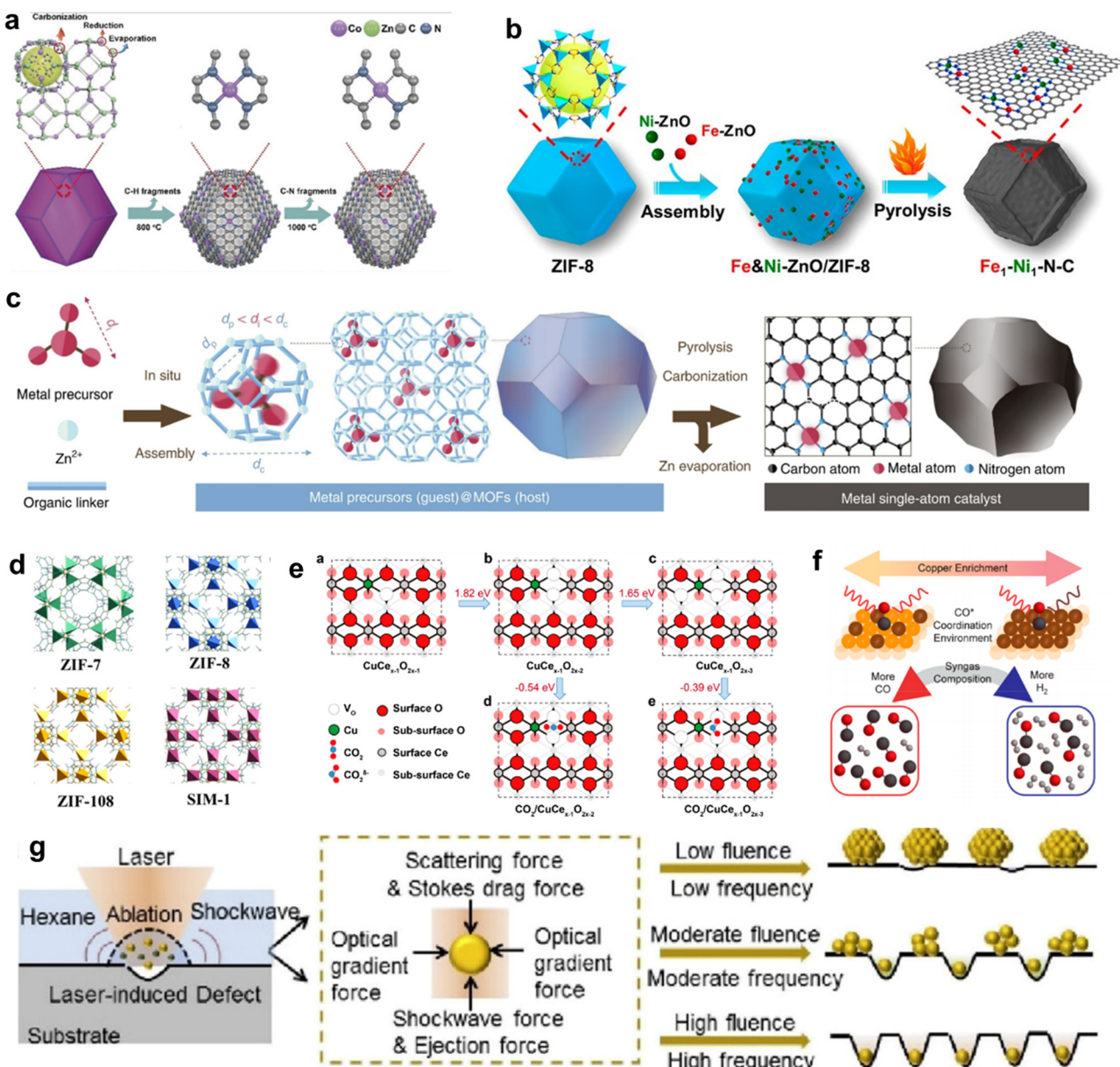

Fig. 4 (a) The formation process of Co–N$_4$ and Co–N$_2$.[86] (b) Schematic illustration for the construction of Fe$_1$–Ni$_1$–N–C with neighbouring Fe and Ni single-atoms based on ZIF-8.[89] (c) Scheme of the host–guest strategy for the fabrication of isolated metal single-atom-site catalysts.[100] (d) The model structures of ZIF catalysts.[102] (e) Theoretical calculations of the most stable structures of Cu-doped CeO$_2$(110) and their effects on CO$_2$ activation.[106] (f) Scheme depicting the relationship between the Cu-enriched Au surface, *in situ* characterization of CO* coordination, and syngas composition.[113] (g) Schematic diagram depicting the synthesis of Pt nanoparticles, Pt clusters, and Pt single atoms under laser planting with low, moderate, and high fluences and frequencies, respectively.[118]

with the characteristic that Zn-based nitrogen-doped carbon is easily converted into a Zn–N$_3$ structure at high temperature.[87] The uniformly dispersed Ni–N$_3$–C with a metal loading of 0.85 wt.% was obtained, which had a lower *COOH free energy than Ni–N$_4$–C. The coordination structure of SACs can also affect the CO$_2$RR performance. By replacing part of the Zn^{2+} sites on nitrogen-doped carbon nanotubes with Ni^{2+}, Hou et al. developed Ni SACs for the efficient conversion of CO$_2$ to CO.[88] By direct pyrolysis of metal–organic frameworks (MOFs) assembled with Fe and Ni-doped ZnO nanoparticles, Jiao et al. precisely constructed a novel Fe$_1$–Ni$_1$–N–C catalyst, with neighboring Fe and Ni single-atom pairs decorated on a nitrogen-doped carbon support (Fig. 4b).[89] The unique architecture of the carriers facilitates the design of the local coordination environment for SAC active sites. Using covalent organic frameworks (COFs) as supports, the metal active sites in SACs can be uniformly dispersed on the multidimensional structure with a high specific surface area, thus the catalysts typically display excellent conductivity and conduction efficiency.[90–92] MOFs have great potential for application in the CO$_2$RR because of their well-defined metal nodes, tunable organic ligands and ordered pore structure.[93,94] The preparation of SACs using MOFs can follow two strategies. First, catalytic organometallic complexes or inorganic metal species are immobilized into MOF pores. Second, the single metal sites are intrinsically created into metal nodes and metallolinkers within frameworks during and before the synthesis process. With MOF carbonization and by firmly embedding single atoms into the carbon skeleton through robust metal–heteroatom (N, O, or S) coordination bonds, SACs with exceptional features and applications can be obtained.[95]

In recent years, a variety of metal SACs have been successfully synthesized using the coordination design strategy. However, the relationship between the coordination structure of SACs and the performance of CO$_2$RR is not sufficiently clear. To design CO$_2$RR electrocatalysts with high activity and selectivity, the structure–performance relationships need to be further investigated.

3.1.2 Spatial confinement strategy. Spatial confinement has been developed as an effective strategy for constructing SACs with precisely defined microenvironments. The best carriers for encapsulation are porous materials such as zeolites, COF, MOFs/zeolite imidazolium salt frameworks (ZIFs), and porous carbon matrices (PCM).[96–99] Li et al. developed a general host–guest strategy for preparing various metal SACs on nitrogen-doped carbon (M/CN, M = Pt, Ir, Pd, Ru, Mo, Ga, Cu, Ni, Mn) (Fig. 4c).[100] The activity of Ir$_1$/CN is 16 times and 19 times that of Pd/C and Pt/C, respectively. In addition, Ir$_1$/CN showed high tolerance to CO poisoning. Zhao et al. prepared a catalyst containing single Ni sites using MOFs for efficient electrocatalytic reduction of CO$_2$.[101] This synthesis is based on ion exchange between Zn nodes and Ni ions adsorbed in the MOF cavity. Jiang et al. studied ZIF-8, ZIF-108, ZIF-7, and SIM-1 with the same SOD (sodium salt) topology and different CO$_2$RR organic ligands in an aqueous solution (Fig. 4d).[102] In situ XAS measurements and density functional theory (DFT) calculations

show that the imidazolate ligand coordinated with the Zn(II) center in ZIFs is the active site of the CO$_2$RR. DFT calculations suggest that ZIF-8 is the most ideal catalyst for catalyzing the CO$_2$RR. ZIF-8 is currently the most extensively used porous MOF precursor for the preparation of SACs, as its derivative porous N-doped carbon has abundant N sites that can anchor individual atoms. Li et al. prepared nickel-metal catalysts of different sizes: from single atoms to more than 100 nm.[103] The suspension obtained after mixing Ni(NO$_3$)$_2$ with ZIF-8 was centrifuged, and the powder thus obtained was calcined at 1000 °C for 2 h; the Ni precursor was converted into Ni single atoms, and ZIF-8 into N-doped carbon support. For Ni metals with different sizes, the CO$_2$RR performance is also different. Ni SAC has an excellent FE for CO. Adli et al. used ZIF-8 to confine the FeN$_4$ site for the CO$_2$RR.[104] For FeN$_4$ sites, the porosity, catalytic surface area, and carbon carrier graphitization were optimized by designing particle size and Fe doping, thereby changing the morphology of the catalyst. The intrinsic activity is controlled using different pyrolysis temperatures, which affects the length and local strain of the Fe–N bonds. DFT calculations suggest that there is a close relationship between the enhancement in intrinsic activity of the CO$_2$RR and the optimized local strain of Fe–N bonds. Hai et al. identified GAFRUDs, CAJQEL, and cg400449c as potential catalysts for electrocatalytic CO$_2$RR through multistep high-throughput screening of the Computational Ready Experiment (CoRE) MOF database, including structural plausibility checks, pore size screening, adsorption capacity prediction, open metal site identification, CO$_2$ molecule activation capacity, and reaction path calculations.[105] In addition, on the basis of DFT calculation, they propose that the polarity of the coordination bond between the metal atom and the coordination atom in the ligand would significantly affect the activation of CO$_2$ molecules, which could provide effective guidance for the rational design of MOF-based CO$_2$RR electrocatalysts. Furthermore, they proposed that the polarity of the coordination bonds between the metal atoms and the coordinating atoms in ligands has a significant impact on the activation of CO$_2$ molecules, and the selectivity for HCOOH mainly depends on the adsorption energy difference between *HCOO and *COOH, which could provide guidelines for the rational design of MOF-based electrocatalysts for the CO$_2$RR.

In summary, the spatial confinement strategy could significantly suppress the migration and aggregation of metal atoms within the porous carrier, while the synergy between the metal single-atom sites and the shape-selective carrier improves the CO$_2$RR performance. The key issue in using this strategy is the selection of suitable metal precursors and support materials with uniform cage/pore sizes to ensure metal species confinement.

3.1.3 Defect design strategy. Isolated single metal atoms can be stably anchored on supports through the design of surface defects, which have been developed as an effective method for synthesizing SACs. Various vacancies and coordination-unsaturated sites are often used not only to trap and stabilize metal single atoms, but also to alter the surrounding

coordination environment.[57,58] Typically, oxygen vacancies in metal oxides have proved ideal sites to anchor metal single atoms. For instance, Cu single-atom sites coordinated with three nearby oxygen vacancies on CeO_2 nanorods have been successfully prepared using a wet impregnation method (Fig. 4e).[106] Multiple oxygen vacancy-bound Cu sites yield a highly effective catalytic center for CO_2 adsorption and activation. Nitrogen vacancies have also been developed to anchor metal single atoms through defect engineering in nitrides. Nitrogen vacancies induced by microwave plasma have been reported to trap Ni atoms and build highly defective Ni-pyridinic N_2 moieties for electroreduction of CO_2 to CO. The unsaturated Ni SAC has a lower energy barrier for the formation of intermediates COOH* and CO*, and exhibits high intrinsic activity towards the CO_2RR.[107] Carbon-based materials are often used as support materials for SACs. Carbon supports are activated with abundant defects and different functional groups on the surface to stabilize metal ions. Xie et al. synthesized kilogram-scale single-atom $Sn^{\delta+}$ on N-doped graphene through a rapid freeze-drying–calcination method. The mixture solution of graphene and metal salts was quickly frozen to disperse Sn ions onto graphene oxide. The freeze-dried samples were calcined in a mixed Ar–NH_3 atmosphere, which is beneficial for N doping into the graphene to stabilize Sn atoms.[108] Graphdiyne (GDY) has also been used as the support to construct SACs.[109,110] The formed Cu–C_4 moiety has a hybridization orbital between the Cu atom and the graphite alkyne carbon to avoid aggregation of Cu single atoms. In addition, the GDY support could be tailored by introducing electron-withdrawing and -donating groups (–F, –H and –OMe) to synthesize GDY derivatives, and their electronic structures are precisely perturbed by the neighboring functional groups.[109] Thus, the charge transfer between GDY and the atom sites could be regulated to optimize the product selectivity of the CO_2RR. Defective metal sites such as metal vacancies and coordination-unsaturated sites can also serve as "traps" to anchor isolated metal atoms. Chen et al. report that $Pd_{10}Te_3$ alloy nanowires can form rich Te defects on the surface after etching by NaOH solutions, which is conducive to the formation of stable and unique Cu_1^0–Cu_1^{x+} atom-pair catalysts.[111] Moreover, a site-specific underpotential electrochemical deposition (UPD) strategy has been developed to synthesize single-atom Cu deposited on defective sulfide-derived Ag nanowires. The defective Ag catalyst and the neighboring Cu atom are stabilized through interfacial interactions.[112]

In general, the construction of atomically dispersed metal catalysts through defect engineering has proven to be an effective strategy. The type and quantity of defects significantly affect the stability and electronic structure of single atom active centers.[20] Therefore, facile and effective methods of defect construction still need to be developed. In addition, it is of great significance to investigate the formation mechanism of isolated catalytic centers at defect sites for the design of SAC catalyst configuration and the synthesis of high-loading SACs.

3.1.4 Other strategies. Other than the strategies discussed above, there have been several more novel synthesis strategies proposed for preparing SACs. As a simple but efficient strategy, electrochemical deposition has been widely used to prepare SACs for the CO_2RR. Ross et al. employed an underpotential deposition method to tune a nanostructured Au electrocatalyst using Cu atoms (Fig. 4f).[113] This method provides a quantitative and systematic means, by which the ratio of surface Cu can be finely controlled. Xuan et al. employed an electroplating method to deposit single atoms of precious metals on various 2D materials. With this method, the doping sites were precisely located at Mo- and S-vacancies, and the surface atomic loadings for Pt, Au, and Cu reached up to 1.1, 7.0, and 14%, respectively.[114] Wang et al. demonstrated a voltage-gauged electrofiltration method to fabricate Fe SAC from a bulk Fe plate.[115] The bulk Fe plate worked as the counter electrode, and were converted into Fe^{2+} under a positive potential. With the assistance of graphene oxide film, the diffusion rate of Fe^{2+} is greatly reduced, resulting in an ultra-low concentration of Fe^{2+} around the working electrode, which successfully prevented the growth of nuclei and the aggregation of metal atoms. Therefore, Fe single atoms were uniformly anchored onto the prepared nitrogen-doped carbon.

Chemical vapor deposition is a novel method for synthesizing single atoms, Qu et al. developed a gas-migration/NH_3-mediated strategy to convert bulk materials (Cu, Co or Ni) directly into single atoms.[116] At high temperatures, ammonia molecules were used as a medium to drag metal atoms out of bulk metal to form gas-phase complexes, then the complex molecules were captured by defects on the nitrogen-rich carbon support, forming isolated metal sites. Considering that the corrosiveness of NH_3 would pose stringent requirements on the equipment, a new gas-migration strategy that employed volatile metal oxides as a single atom source was demonstrated.[117] At high temperatures, metal oxides were evaporated to generate gaseous species, which were transported onto nitrogen-doped carbon and anchored by defects to form isolated metal atom/NC catalysts. Recently, a novel one-step laser-planting strategy was employed to create a set of high-density SACs on various supports, including carbon black, graphene quantum dots, metals, and oxides (Fig. 4g).[118] The laser pulses created defects on the support and simultaneously decomposed the precursors into metal atoms, which were subsequently immobilized on the as-produced defects via electronic interaction. Using this strategy, a high loading of single atoms of 41.8 wt.% has been achieved.

In addition to the above-mentioned synthesis methods, a few other special strategies have been proposed including nanoparticles becoming single atoms via solid diffusion,[119–121] solid-state atom diffusion,[122,123] in situ thermal atomization methods,[119] electrospinning polymer nanofibers,[124] and cross-linking and self-assembly of graphene quantum dots.[125]

3.2 Characterization techniques of SACs

Upon providing an overview of the synthesis strategies for SACs, determining the geometric structure and electronic environment of SACs is crucial for investigating their structure–function relationship in CO_2RR applications. Primarily, ascertaining the

geometric structure enables the provision of compelling evidence to discern between SACs and nanoparticle catalysts, thus illuminating the intricate coordination configuration inherent in SACs. Concomitantly, delving into the electronic environment facilitates the acquisition of critical data concerning the electron orbitals and oxidation states of catalytic active centers. While a plethora of techniques exist for material characterization, such as X-ray diffraction (XRD), X-ray photoelectron spectroscopy (XPS), Raman, and others, their applicability may fall short in fulfilling the exigencies of atomic-resolution structural characterization of SACs. In contrast, characterization techniques tailored expeditiously for resolving the geometric/electronic structures of SACs predominantly involve AC-HAADF-STEM, XAS, and Mössbauer spectroscopy. Herein, we will not delve into the details of each characterization technique, but rather focus on discussing the distinct characterization techniques tailored for SACs.

3.2.1 AC-HAADF-STEM. Transmission electron microscopy (TEM) stands as one of the most ubiquitous techniques employed for visualizing material morphology. Nevertheless, when dealing with SACs boasting atomic-level resolution, a more sophisticated characterization methodology is in demand to discern delicate morphologies with precision. In recent years, owing to the thriving advancements witnessed in SACs, AC-HAADF-STEM has emerged as an indispensable characterization technique for atomically dispersed active sites in SACs. AC-HAADF-STEM is commonly employed to characterize metal atoms loaded on solid supports. Due to the stronger electrostatic interaction between the metal atomic nucleus and the incident electron beam, atoms with higher atomic numbers (Z)

can scatter more electrons at higher angles. Consequently, metal atoms possessing higher Z values manifest as heightened contrasts relative to their supporting substrates, thus facilitating clearer delineation of their atomic configurations.[64] This phenomenon is particularly pronounced in SACs on carbon-based substrates, given the stark contrast in Z between metal single atoms and the carbon support. A seminal exemplification in this regard is the work by Chung *et al.*, who reported a Fe SAC supported on carbon and directly observed the Fe–N$_4$ configuration for the first time by using AC-HAADF-STEM combined with electron energy-loss spectroscopy (EELS) characterization techniques (Fig. 5a and b).[126] This study provided crucial guidance for subsequent structural analysis of M–N–C catalysts at the atomic level and their investigation across various catalytic applications.

3.2.2 XAS. AC-HAADF-STEM is capable of visualizing single metal atoms loaded on solid supports, particularly carbon supports, by utilizing their different Z contrasts. However, it does not provide information regarding the electronic states and coordination configurations of the metal active sites. In contrast, XAS (including X-ray absorption near edge structure (XANES) and extended X-ray absorption fine structure (EXAFS)) is a powerful technique for characterizing the electronic states, coordination and geometric structures of metal active sites.[64] XANES is sensitive in capturing information related to average valence states and electron configurations. The near-edge position in XANES corresponds to the oxidation state of the target element, where higher oxidation states require greater energy to excite core electrons. On the other hand, EXAFS provides crucial details about the local geometry and coordination
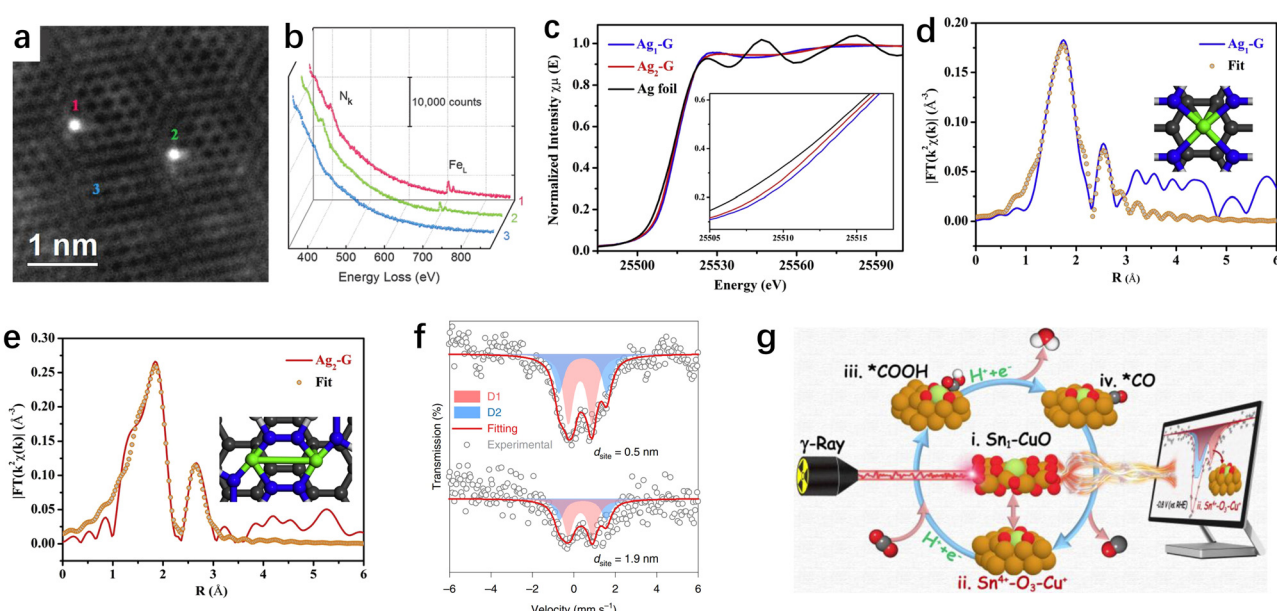
Fig. 5 (a) AC-HAADF-STEM image of individual Fe atoms (labelled 1, 2, and 3) in a few-layer graphene sheet.[126] (b) EEL spectra of the N k-edge and Fe L-edge acquired from single atoms (1 and 2) and few-layer graphene (3).[126] (c) Ag K-edge XANES spectra (inset is the expanded view of the rising edge).[127] EXAFS R-space fitting curves for Ag1−G (d) and Ag2−G (e), respectively. The inset of (d) and (e) is the schematic model of Ag1−G and Ag2−G, respectively (Ag in green, N in blue, and C in gray).[127] (f) Iron-57 Mössbauer spectroscopy of two catalysts with d_{site} = 0.5 and 1.9 nm. The curves were offset for clarity.[129] (g) ^{119}Sn Mössbauer spectroscopy as a probe technique to track the catalyst's metastable species.[130]

environment of the single atomic sites. By fitting the results from EXAFS, important parameters such as bond length and coordination numbers can be inferred. Additionally, the bonding and coordination configuration of the metal centers can also be reasonably deduced through the analysis of EXAFS data. We previously reported a method for customizing metal active sites, wherein we pre-synthesized mononuclear and binuclear Ag complexes as metal precursors. These precursors were then dispersed on graphene (G) to successfully synthesize Ag1–G and Ag2–G catalysts.[127] Combining the customized synthesis strategy with XAS results, and conducting a detailed analysis of other test results along with fitting of EXAFS data, we have confirmed that the coordination configurations of the active centers in Ag1–G and Ag2–G catalysts are Ag–N_4 and AgN_3–AgN_3 structures, respectively (Fig. 5c–e).

3.2.3   Mössbauer spectroscopy. Mössbauer spectroscopy is an effective technique used to probe the coordination structures and spin states of various Mössbauer-active metal centers (such as Fe, Sn, Sb, *etc.*) in SACs.[128] Under ambient temperature testing conditions, normally the nuclear transitions of ^{57}Fe and ^{119}Sn have a higher probability of exhibiting the Mössbauer effect. Currently, research utilizing Mössbauer spectroscopy to investigate the electronic states of SACs is predominantly focused on the elements Fe and Sn. Jin *et al.* conducted a study where they designed Fe–N_4 catalysts with varying densities of single-atom active sites, aiming to investigate the influence of inter-site distances on the properties of Fe–N_4.[129] Through Mössbauer spectroscopy testing, the results demonstrated that at inter-site distances of 0.5 and 1.9 nm in Fe–N_4, the deconvoluted transmission profiles provided evidence that D1 and D2 doublets dominate most Fe species for the two samples (Fig. 5f). Notably, D1 was assigned to the low-spin Fe(II)–N_4 species acting as a highly active catalytic site, whereas D2 was associated with a medium-spin Fe(II)–N_4 species. Chen *et al.* reported a copper oxide-supported atomically dispersed Sn catalyst for the CO_2RR.[130] In their study, they employed ^{119}Sn Mössbauer spectroscopy as a probe technique to track the catalyst's metastable species. The Mössbauer spectroscopy results revealed that the atomically dispersed Sn^{4+} sites on the CuO substrate underwent a transformation from Sn^{4+}–O_4–Cu^{2+} to a metastable state of Sn^{4+}–O_3–Cu^+ during the CO2RR (Fig. 5g)

4. Structure–function relationship of SACs in electrochemical CO_2RRs

4.1   Coordination environment regulation

The coordination environment of SACs can directly influence the electronic and geometric structure of the metal active site, thereby altering the adsorption/desorption processes of key intermediates in the CO_2RR. Additionally, different coordination environments can result in distinct microenvironments for the CO_2RR, such as interfacial water and local pH, playing a significant regulatory role in the reaction process. In this section, we primarily focus on the discussion of two types

of coordination regulations: in-plane and out-of-plane coordination.

4.1.1   In-plane coordination. Regulation of the in-plane coordination environment typically involves the control of atoms in the first shell of the metal active site, which allows for a direct modification of the oxidation state or electronic structure of the metal centers.[131] As is well known, Fe SACs with FeN_4 sites exhibit a lower CO_2RR reduction onset potential and can efficiently electrochemically reduce CO_2 to CO at low potentials. However, this high activity and selectivity rapidly decrease as the potential increases, and high CO selectivity can only be achieved within a narrow voltage range. The main reason for this is the adsorption equilibrium issue of *COOH and *CO key intermediates on Fe SACs (with a higher formation energy barrier for *COOH and stronger adsorption of *CO). To this end, Zhao *et al.* replaced N with O atoms and synthesized Fe SACs with a unique FeN_2O_2 coordination structure using a strategy of thermal decomposition of oxygen-containing MOF precursors (Fig. 6a).[132] Compared to N, O atoms have higher electronegativity and show tremendous potential in regulating the reaction kinetics. The synthesized FeN_2O_2 catalyst showed over 95% selectivity within the voltage range of −0.4 to −0.8 V. Theoretical calculations indicated that, with O coordination, the Fe sites exhibited a lower formation energy for *COOH and facilitated *CO desorption. Recently, Zhang *et al.* reported for the first time the Ga–N_3S–PC SASC with a flexible structural feature achieved through coordination with S and P.[133] This unique structure enables the Ga active sites to exhibit excellent CO_2RR performance with a selectivity of over 90% towards CO. Theoretical simulations suggest that the Ga–N_3S–PC sites can undergo structural transformations and oscillations during the reaction process, optimizing the adsorption energy of *COOH to adapt to the CO_2RR process. Compared to the Ga–N_4 structure, Ga–N_3S–PC exhibits higher activity and stability.

H_2O is a molecule that directly participates in the reaction, generating H through dissociation for the PCET process. Therefore, it is crucial to regulate the interfacial water for efficient CO_2RR.[134] In this regard, besides directly adjusting the electronic structure of the metal center by optimizing the first coordination sphere, controlling the interfacial microenvironment through non-coordinating heteroatom doping also has significant importance in the development of high-performance SACs. For example, in order to promote the synergistic adsorption and activation of CO_2 and H_2O, Liu *et al.* constructed a SASC with FeN_4/graphitic N atomic interface sites through a H_2-assisted pyrolysis strategy, which achieved a CO faradaic efficiency of over 90% within the range of −0.3 to −0.8 V.[135] *Operando* attenuated total reflection surface enhanced infrared absorption spectroscopy (ATR-SEIRAS) and the first-principle calculations indicate that the presence of graphitic N sites facilitates the co-adsorption of H_2O, thereby promoting the activation of CO_2 and its conversion into the key intermediate *COOH (Fig. 6b). In another work, Sun *et al.* achieved efficient electrochemical CO_2 to CO conversion on Mo SACs through the incorporation of Se into the carbon support.[136] The study
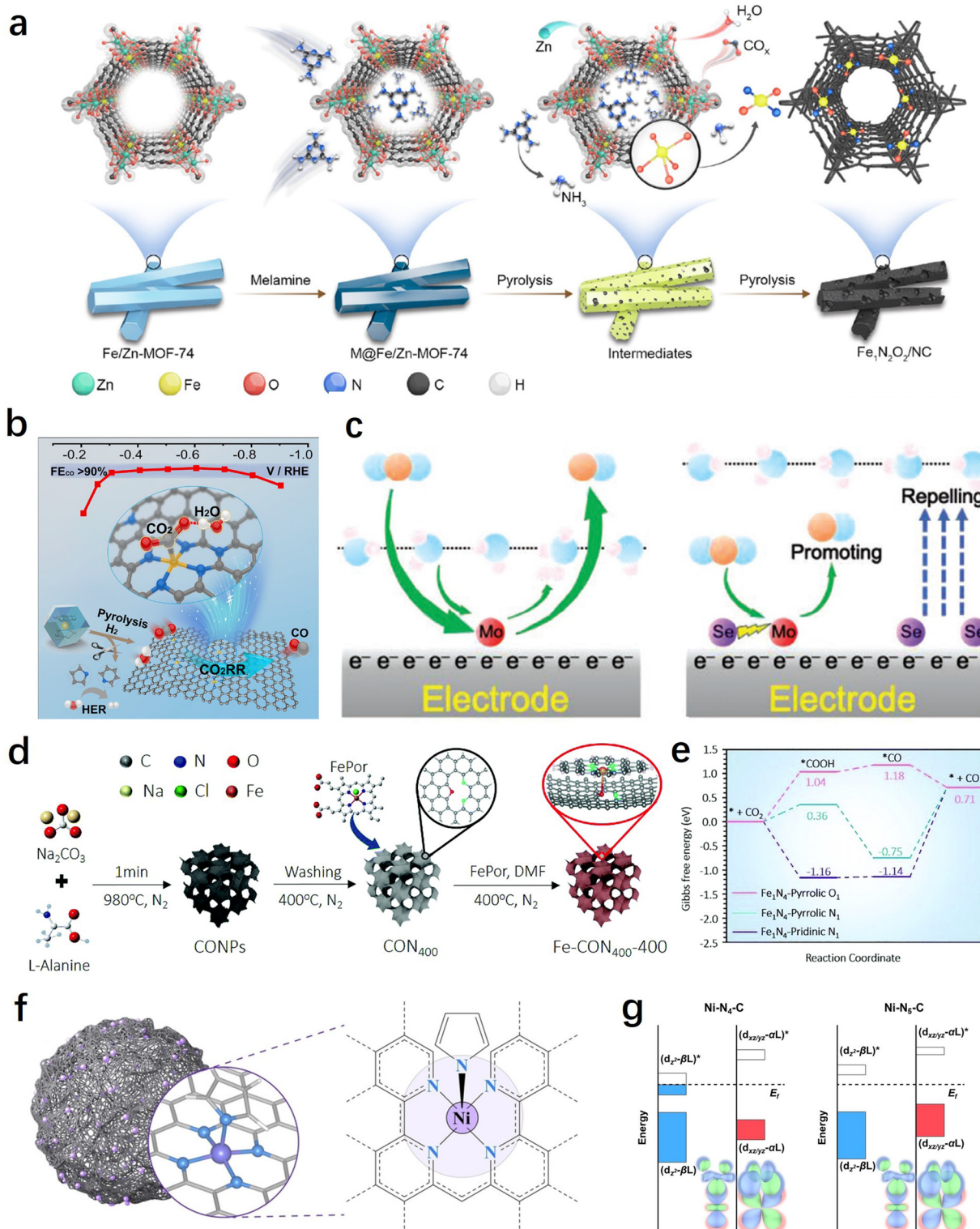
Fig. 6 (a) Schematic illustration of the preparation of $Fe_1N_2O_2/NC$.[132] (b) Synthesis method and CO_2RR performance of H_2-FeN_4/C.[135] (c) Schematic diagram of the reaction mechanism of MoSA–SeSA.[136] (d) Schematic of the synthetic process for well-designed iron single-atomic catalysts.[138] (e) CO_2RR pathways on Fe sites of different catalyst configurations.[138] (f) Schematic of the single-atom nanozyme Ni–N_5–C.[140] (g) Orbital interactions between Ni centers (d_{z^2}, $d_{xz/yz}$) and adsorbed COOH on Ni–N_4–C and Ni–N_5–C.[140]

demonstrates that the introduction of neighbouring Se (6.0 Å) can effectively improve the reaction thermodynamics of the

MoN_4 sites through long-range electronic interactions, promoting *CO desorption. On the other hand, the remaining Se far

away from Mo SACs (>8.5 Å) can improve the electrode/electrolyte interface by repelling water molecules to suppress the hydrogen evolution reaction (HER), thereby enhancing the selectivity of the CO$_2$RR (Fig. 6c).

4.1.2 Out-of-plane coordination. The introduction of axial coordinating atoms can further enrich the coordination environment of the active site in SACs. When they form special configurations by coordinating and bonding with the metal atom center, they can regulate the spin state and electronic properties such as the d-band center of the metal sites.[137] This, in turn, allows for modulation of the binding energy between the active site and reactants/intermediates, ultimately achieving control over the intrinsic catalytic activity of the catalyst. By employing a rapid pyrolysis and controlled activation strategy, a FeN$_4$–O$_1$ site with axial O coordination was successfully synthesized by Chen and co-workers (Fig. 6d).[138] The results indicate that the introduction of axial O can induce enhanced electron localization at the Fe site, thereby promoting the desorption of *CO and increasing the energy barrier for competitive HERs (Fig. 6e). The synthesized FeN$_4$–O$_1$ SACs demonstrate nearly 100% CO selectivity within a wide potential window (310 mV). Using a similar approach, Pan et al. successfully constructed SACs with a unique Co–N$_5$ coordination structure. Thanks to its lower *COOH formation energy and facilitated *CO desorption process, this catalyst exhibits an excellent electrochemical conversion efficiency of CO$_2$ to CO.[139]

From the above results, it can be observed that high selectivity in electrochemical CO$_2$-to-CO conversion has been achieved through the coordination structure and electronic modulation of SACs. However, there are still limitations in terms of current density and catalyst durability. Recently, Huang et al. made a breakthrough in achieving high selectivity, high current density, and sustained catalyst durability through axial coordination engineering.[140] Inspired by natural metalloenzymes, they designed and constructed a single-atom nanoenzyme with a Ni–N$_5$–C structure featuring axial N coordination (Fig. 6f). Compared to the traditional planar Ni–N$_4$ coordination structure, the square-pyramidal NiN$_5$ site's d$_{z^2}$ and d$_{xz/yz}$ orbital energy levels were increased and decreased, respectively (Fig. 6g). This facilitates the adsorption and activation of CO$_2$ molecules and the desorption of CO, greatly enhancing the reaction kinetics. Therefore, the synthesized catalyst achieved a 99.6% CO faradaic efficiency (turnover frequency of 69.7 s^{-1}) at an ultra-high current density of 1.23 A cm^{-2}, and exhibited exceptional stability for 100 hours, surpassing significantly many other reported SACs. In addition to the coordination of N and O, elements such as S, Cl, Br, and I have also demonstrated promising potential in axial coordination engineering.[141,142] Overall, the proposal and development of axial coordination regulation will contribute to further investigations of the mechanism of single-atom catalysts, as well as expanding the strategies and methods for the regulation of SACs.[143,144]

4.2 Diatomic sites regulation

In recent years, DACs have gained extensive attention as extensions of SACs.[145] Compared with SACs, DACs possess more complex and flexible active sites, enabling them to achieve better catalytic performance. This is particularly important for the CO$_2$RR involving various reaction intermediates. When all intermediates are adsorbed on a single active site, it becomes challenging to achieve optimal adsorption states for each intermediate. By constructing bimetallic active sites, the adsorption energy of different intermediates can be optimized, thereby breaking this linear relationship and achieving greater catalytic performance. Furthermore, the construction of diatomic sites has potential for achieving synergistic adsorption and activation of both CO$_2$ and H$_2$O, thereby further enhancing reaction kinetics. In this section, we will categorize DACs into homonuclear diatomic sites and heteronuclear diatomic sites for discussion.

4.2.1 Homonuclear diatomic sites. Fine-tuning interactions in the second coordination shell of enzymes or homogeneous catalysts is crucial for their functionality. Now, this concept has been applied to heterogeneous catalysts, utilizing copper atom pairs for the selective electrochemical reduction of CO$_2$. Jiao et al. reported a copper atom pair catalyst (denoted as Cu-APC) loaded on Pd$_{10}$Te$_3$ nanowires, where the active sites were characterized as Cu$_1^0$–Cu$_1^{x+}$ units through AC-HAADF-STEM, XAS and theoretical calculations.[111] This unique atom pair structure efficiently promotes the activation and conversion of CO$_2$ through a diatomic activating bimolecular mechanism, where the Cu$_1^{x+}$ site acts as a Lewis acid for adsorbing water molecules, and Cu$_1^0$ acts as a Lewis base for adsorbing and activating CO$_2$. This synergistic proton-coupled electron transfer leads to a significant enhancement in the catalytic activity of Cu-APC catalysts (Fig. 7a). The concept of pairing atoms to achieve better performance opens up new opportunities for the design of SACs, where two are better than one when atomic synergies come into play. Similarly, in a recent study, Hao et al. successfully synthesized Ni dual-atom site catalysts through the in situ transformation of Ni nanoparticles.[96] In situ XAS and theoretical calculations revealed that the Ni dual-atom centers can facilitate the adsorption of hydroxyl and form an electron-rich microenvironment at the Ni$_2$ sites during the CO$_2$RR process, and the resulting catalytic microenvironment promotes the formation of *COOH and the desorption of *CO. As a result, the synthesized catalyst achieved a $>99\%$ CO faradaic efficiency at an ultra-high current density of 1 A cm^{-2} (Fig. 7b).

In addition, DACs have demonstrated superior performance and advantages over SACs in the synthesis of multi-carbon products. For instance, by constructing dual-atomic Cu sites, Li et al. successfully achieved efficient production of C$_2$ products (mainly ethylene and acetic acid) on DACs with a high faradaic efficiency of 91% and a partial current density of 90 mA cm^{-2}.[146] Theoretical calculations suggest that the neighboring Cu sites can facilitate the carbon–carbon coupling process of CO. Interestingly, when one of the Cu atoms is replaced by a Ni atom, this highly efficient carbon–carbon coupling pathway is terminated as a result of the excessive CO adsorption by the Ni atom (Fig. 7c). This finding emphasizes the importance of compatibility between bimetallic centers for the CO$_2$RR process.
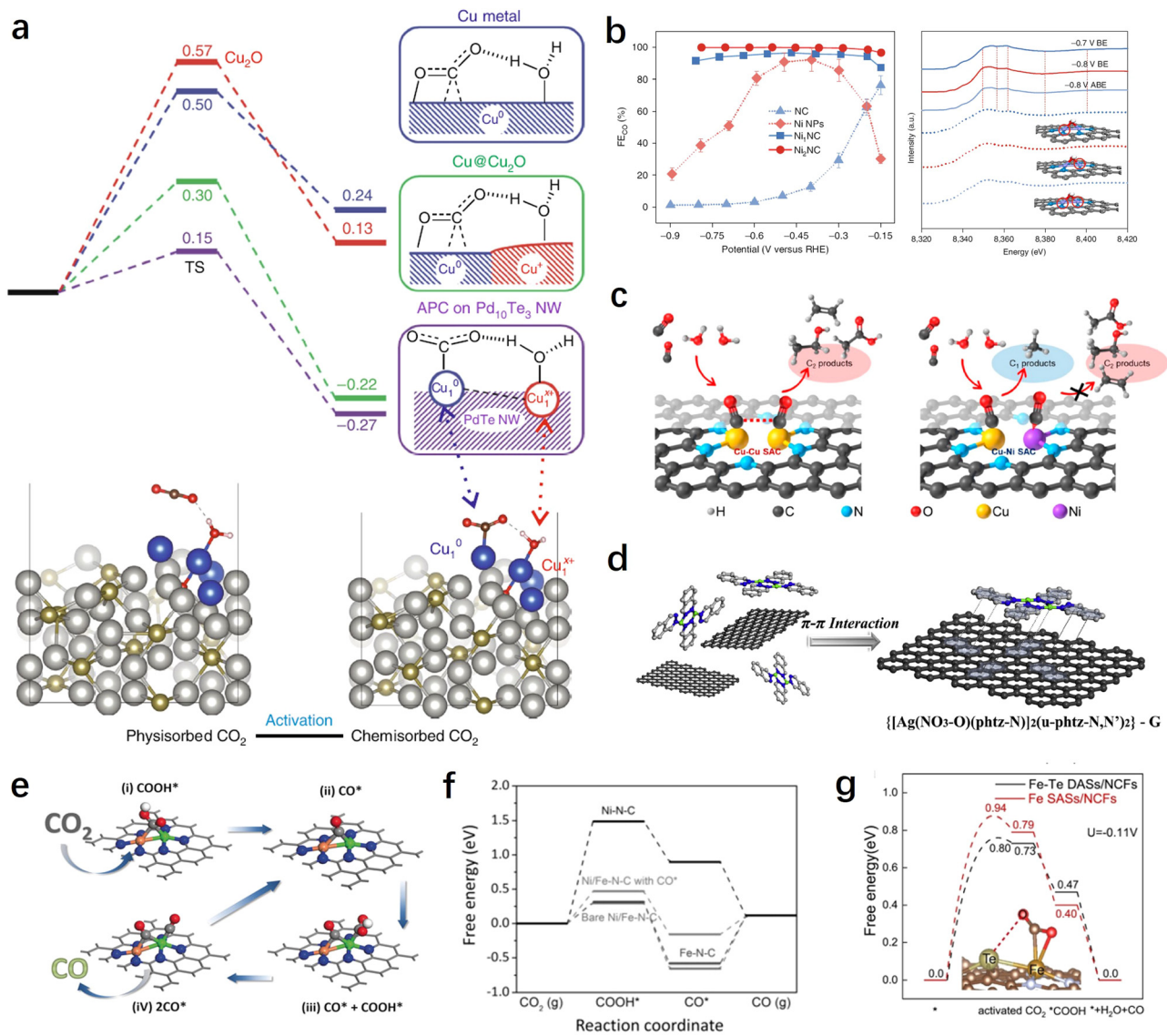
Fig. 7 (a) Free energy profiles for the CO_2 activation mode of Cu-APC catalysts.[111] (b) CO_2RR performance and XANES spectra of Ni_2NC catalysts.[96] (c) Schemes showing the structures and products for the CO_2RR on dual Cu−Cu and Cu−Ni SACs.[146] (d) Schematic illustration of the synthesis process of Ag_2−G catalysts.[127] (e) The catalytic mechanism on diatomic NiFe catalysts based on the optimized structures of adsorbed intermediates COOH* and CO*.[147] (f) Calculated free energy diagrams for the CO_2RR yielding CO on different catalysts.[147] (g) The free energy diagram of the CO_2RR on Fe−Te DASs/NCFs.[149]

Despite some breakthroughs in the activity and selectivity of DACs for the CO_2RR, there are still difficulties and challenges in the precise synthesis and controllable preparation of dual-atomic sites. To this end, Li *et al.* have developed a dual-core metal molecular pre-synthesis and post-adsorption strategy.[127] They first synthesized a well-defined binuclear Ag complex and then obtained DACs with AgN_3–AgN_3 sites through the π–π interaction between the complex and graphene, as well as low-temperature treatment (Fig. 7d). These AgN_3–AgN_3 sites demonstrated greater advantages in synergistic adsorption and activation of CO_2 compared to single Ag sites.

4.2.2 Heteronuclear diatomic sites. The synergistic effect of bimetallic interactions occurs not only between two identical metal atoms but also between two different metal atoms.

The coordination of d orbitals between heteronuclear metals allows for flexible modulation of the active center, reducing energy barriers, and thereby generating unexpected catalytic performance. For example, the rate-determining steps for the CO_2RR on Ni−NC and Fe−NC are $CO_2(g) \rightarrow$ *COOH and *CO $\rightarrow$ CO(g), respectively, due to the weak adsorption of *COOH on Ni−NC and strong adsorption of *CO on Fe−NC. This naturally leads to a reasonable conjecture and consideration: can their advantages in the reaction be maximized by combining them to achieve an optimal performance? Based on this, Ren *et al.* ingeniously designed an isolated bimetallic Ni−Fe site.[147] Studies have shown that during the CO_2RR process, the bimetallic Ni−Fe center undergoes structural evolution to a CO-adsorbed moiety, which greatly reduces the formation energy

barrier of *COOH and promotes the adsorption of *CO (Fig. 7e and f). As a result, the synthesized bimetallic Ni–Fe catalyst exhibits superior electrochemical CO_2 to CO activity. The design strategy for this heteronuclear diatomic pair has also been successfully applied to Co–Cu diatomic site catalysts.[148] Because of the weak binding of *COOH on Cu–SAC, a high energy input is required for CO_2 activation to *COOH. On the other hand, Co–SAC exhibits strong *COOH adsorption and enhanced *CO binding strength. When combined, CoCu–DASC(Co) exhibits a relatively moderate d-band center value compared to Co–SAC and Cu–SAC. This implies that the adsorption strength of intermediates on the CoCu bimetallic sites is moderately balanced. As a result, the prepared diatomic CoCu catalyst can maintain over 95% CO selectivity in the range of 100 mA cm^{-2} to 500 mA cm^{-2}, with a maximum CO partial current density of 483 mA cm^{-2}, far exceeding the industrial current density requirement (>200 mA cm^{-2}).

Modulating the activation mode of CO_2 molecules through synergistic effects between neighboring atoms is an attractive yet challenging strategy. Pan et al. utilized neighboring Te atoms to induce and regulate the Fe site and constructed Fe–Te diatomic sites for synergistic CO_2RRs.[149] The results demonstrate that the low-valent Fe$^{\delta+}$ forms bonds with one carbon and one oxygen atom of the CO_2 molecule, while the adjacent Te$^{\delta+}$ acts as an electron donor, regulating the electronic structure of the Fe$^{\delta+}$ site and stabilizing the other oxygen atom of the CO_2 molecule. This enhances the $2\pi_u$ orbital interaction of CO_2 and makes the CO_2 molecule more prone to bending, thereby reducing the activation barrier and improving the CO_2RR performance (Fig. 7g). In addition to transition metals and main group metals, rare earth metals have shown significant potential in modulating the catalytic activity of metal sites and activating CO_2 due to their unique electronic structure and catalytic properties. Therefore, designing and constructing heteronuclear diatomic sites containing rare earth elements show promise for further tuning the reaction pathways and performance of CO_2RRs. For instance, Liang et al. synthesized atomically dispersed InCe/NC catalysts using a one-step method.[150] Experimental results demonstrated that the introduction of Ce promotes the electrochemical conversion of CO_2 to formate, while the conversion of CO and the hydrogen are suppressed. Theoretical calculations revealed that the incorporation of single Ce atoms not only significantly facilitates electron transfer but also optimizes the In-5p orbitals, enhancing the adsorption energy of the key intermediate *OCHO on the In sites along the formate pathway.

4.3 Tandem catalytic regulation

Currently, electrochemical CO_2 reduction for the production of simple 2e$^-$ products such as CO or formate has achieved high selectivity and activity, particularly when utilizing single-atom catalysts. However, significant challenges persist in the production of hydrocarbons or alcohols from the CO_2RR. It is generally understood that the conversion of CO_2 to multi-electron deep reduction products typically involves a two-step sequential process:[151] (1) CO_2 reduction to CO; (2) further reduction of

CO to obtain deep reduction products. The electrochemical CO_2 reduction process comprises multiple coupled or consecutive proton-electron transfer steps, and the design and synthesis of tandem catalytic systems using single-atom catalysts as CO-forming or water activation sites show significant potential for facilitating the production of high-value products in these two steps.

4.3.1 SACs serving as CO formation centers. Theoretical studies have revealed that the overall selectivity of C_{2+} products is largely dependent on the reaction kinetics of *CO–*CO coupling, which is directly proportional to the square of the *CO coverage. While the *CO coverage can be enhanced by improving local CO concentration.[152,153] As discussed above, SACs exhibit exceptionally high selectivity and activity in the process of CO_2 reduction to CO. Utilizing SACs for the first step in tandem catalysis, converting CO_2 to CO, and subsequently coupling it with CO to other product catalytic sites (such as copper), has great promise for the electrochemical reduction of CO_2 to multi-electron deep reduction products.

The potential matching between different materials needs to be carefully considered prior to designing such a tandem catalytic system, where the high selectivity generation of CO and subsequent C–C coupling processes need to be simultaneously achieved at a specific potential. Generally, for Cu-based catalysts, C–C coupling often occurs at relatively negative potentials (>-1 V vs. RHE). Therefore, it is essential for SACs to have a broad potential range while maintaining a high CO faradaic efficiency. According to reports, Ni SACs have been shown to maintain a CO selectivity of over 97% even at -2.4 V vs. RHE, making them an ideal candidate material for these tandem catalytic systems.[140] For instance, Yin et al. prepared hybrid tandem catalysts by combining Ni single atoms loaded on high surface area carbon supports with Cu nanowires (Fig. 8a).[154] In situ SEIRAS studies revealed that the incorporation of Ni single atoms significantly enhanced the enrichment of CO on the Cu surface, thereby facilitating the C–C coupling process. By adjusting the ratio of hybrid components, the optimized catalyst achieved a 66% ethylene faradaic efficiency in a flow-cell device, which was improved by five times compared to pure copper. Similarly, Meng et al. prepared a non-precious metal-based tandem electrocatalyst, PTF(Ni)/Cu, by anchoring Ni single atoms and loading Cu nanoparticles onto a porphyrin-based triazine framework.[155] During the CO_2RR process, the single-atom Ni efficiently reduces CO_2 to the intermediate CO, which is immediately converted to ethylene through highly efficient C–C coupling reactions catalyzed by nearby Cu particles. Therefore, compared to the non-tandem catalyst PTF/Cu (triazine framework with no metal Ni atoms in the porphyrin center) that mainly produces methane, the faradaic efficiency of ethylene has increased by fivefold (-1.1 V vs. RHE) (Fig. 8b).

Potential matching determines the compatibility of different components, while spatial distribution determines the efficiency of the tandem reaction.[156] The generated CO on SACs often needs to spill over to adjacent Cu sites, and if the distance between them is too far, the tandem process will be hindered.
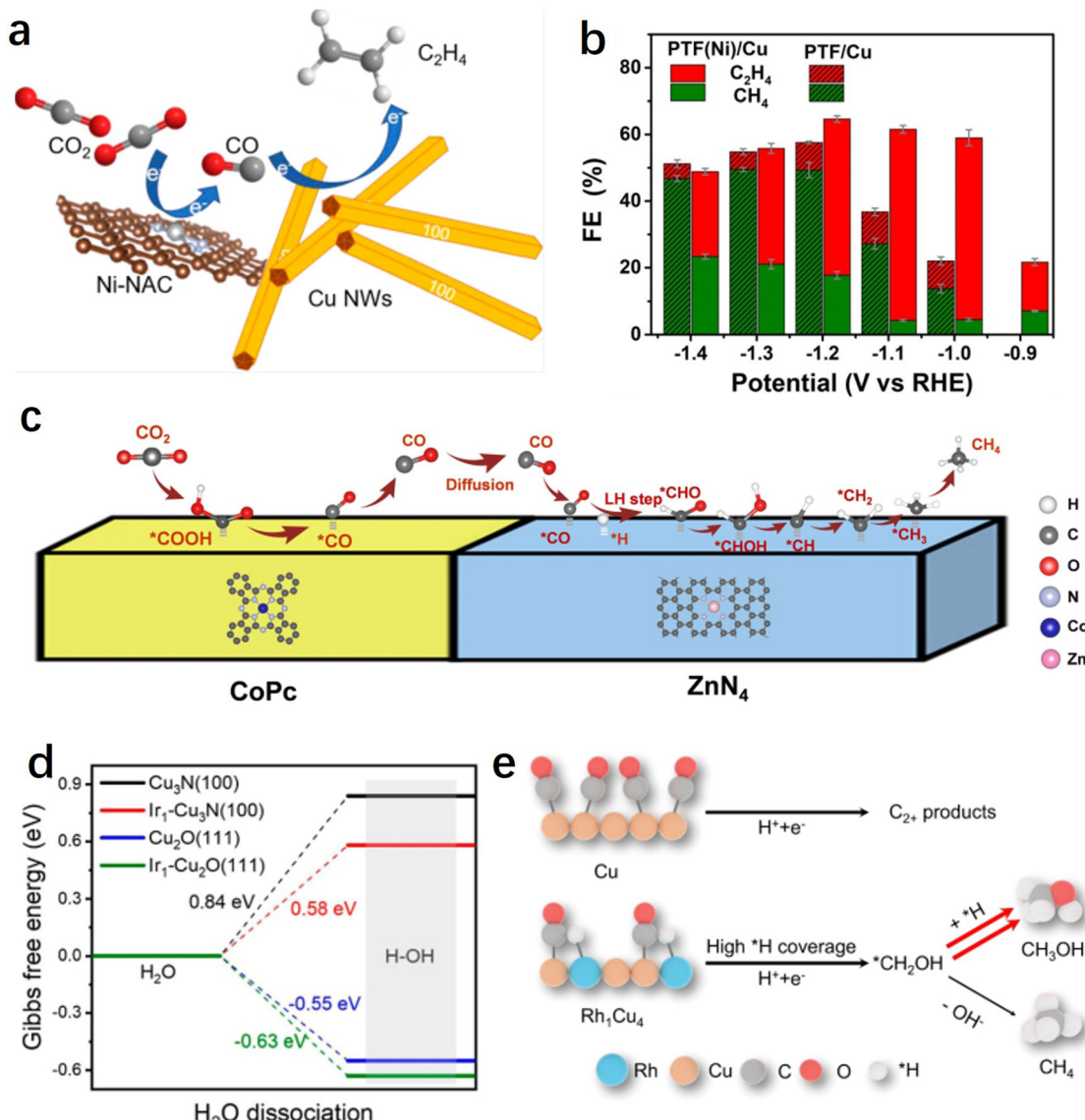
Fig. 8 (a) Schematic diagrams of the tandem systems of Cu/Ni–NAC hybrid catalysts.[154] (b) Faradaic efficiency of C_2H_4 and CH_4 at different potentials on PTF(Ni)/Cu and PTF/Cu.[155] (c) A proposed reaction mechanism for the production of CH_4 over CoPc@Zn–N–C.[158] (d) Calculated ΔG for the H_2O dissociation process.[162] (e) Mechanism of CH_3OH formation on the Rh_1Cu_4 catalyst.[161]

Wang *et al.* systematically studied the influence of spatial distribution between two components on the tandem reaction process.[157] They chose CoPC molecules, known as excellent CO-producing small molecule catalysts, and Cu nanocubes (Cu_{cub}) as a model, and prepared two distinct mixed catalysts. One catalyst was CoPC–Cu_{cub}/C, where CoPC and Cu_{cub} shared an interface; the other was CoPC–C/Cu_{cub}, where CoPC was initially loaded onto carbon black and subsequently mixed with Cu_{cub}. Electrochemical tests revealed that CoPC–Cu_{cub}/C exhibited nearly double the selectivity for C_2 products compared to Cu_{cub}/C, whereas the faradaic efficiency of CoPC–C/Cu_{cub} decreased by half. This outcome elucidates the surface transport mechanism of CO intermediates between the two components of the tandem catalyst, highlighting the importance of their relative spatial distribution for achieving efficient tandem

reactions. In addition to the tandem systems between single atoms and metal Cu, tandem catalytic pathways can also be formed between different single-atom sites. For instance, Lin *et al.* reported a tandem catalytic system using CoPC and Zn–N–C for the deep hydrogenation reduction of CO_2 to produce methane.[158] The research results demonstrated that CO_2 was initially reduced to CO on CoPC, then diffused to Zn–N–C, where it undergoes further reduction to CH_4 at the ZnN_4 site (Fig. 8c). Compared to using CoPC or Zn–N–C alone, the tandem catalyst showed more than 100-fold increase in the CH_4/CO production rate ratio.

4.3.2 SACs serving as water activation centers. The selectivity of specific products is also influenced by the rate-determining step dominated by PCET for the formation of key intermediates. For instance, *CO protonation to *CHO for methanol, methane,

or ethylene production; and *HC–COH protonation to *HC–CHOH for the production of CH_3CH_2OH.[20,159,160] These processes are closely related to the coverage of adsorbed protons (*H_{ad}), which typically originate from the dissociation of water molecules. Therefore, the introduction of atomically dispersed water activation sites can facilitate the dissociation of water molecules to optimize *H_{ad} coverage, thereby promoting the generation of key intermediates. In comparison to metal clusters or particles, atomically dispersed sites may have the advantage of avoiding an excessive increase in *H_{ad} coverage, which could otherwise lead to the promotion of the HER side reaction.[161]

On the reaction pathway of CO_2 reduction to CH_4, the further hydrogenation of the intermediate *CO is often considered the rate-determining step, while the slow water dissociation kinetics limits the rate of proton supply, thereby impeding the electrochemical methanation of CO_2. To address this issue, Chen et al. successfully introduced single-atom Ir into copper-based catalysts, resulting in the synthesis of Ir single-atom-doped Cu_3N/CuO hybrid materials.[162] This hybrid catalyst exhibits exceptionally high methane selectivity and activity (with a 75% methane Faraday efficiency at a current density of 320 mA cm^{-2}), surpassing catalysts lacking Ir single-atom doping. Experimental and theoretical results indicate that Ir single atoms facilitate the dissociation of water into protons and supply them to Cu_3N/CuO sites for the protonation of *CO to *CHO, significantly accelerating the kinetics of CO_2 methanation (Fig. 8d). It has been indicated that methanol and methane products share a common intermediate, *CHO. After overcoming the energy barrier of the rate-determining step along the C_1 pathway (i.e., *CO-to-*CHO), the critical branching step for generating methanol or methane involves either continued hydrogenation (resulting in *CHOH, *CH_2OH) or dehydroxylation (leading to *CH, *CH_2, etc.).[163,164] Therefore, further optimizing the *H adsorption on the catalyst surface shows promise for enhancing methanol selectivity. Building on this insight, Zhang et al. synthesized a Rh-doped Rh_1Cu_4 single-atom alloy catalyst.[161] DFT results demonstrate that isolated Rh sites enhance *H coverage on the Rh_1Cu_4 catalyst and facilitate the hydrogenation of *$CH2OH$, leading to methanol production. The Rh_1Cu_4 catalyst exhibits the highest methanol partial current density of 111.7 ± 12.8 mA cm^{-2} with a Faraday efficiency of 46.2 ± 5.3%. Furthermore, comparative experiments reveal that the introduction of Rh clusters results in excessive *H coverage on the catalyst surface, leading to a decrease in methanol selectivity and an increase in hydrogen production (Fig. 8e). This further shows the advantage of single-atom sites as water activation or *H adsorption sites.

In summary, SACs can promote the supply of CO and protons during the CO_2RR process by facilitating the generation of CO and the dissociation of water. Subsequently, these intermediate products can be captured by another active site in the tandem catalyst, forming *CO and *H_{ad} species, leading to the acceleration of the rate-determining steps involving C–C coupling and PCET.

4.4 Catalyst support regulation

Choosing the appropriate support material is essential to providing strong binding through ion or covalent interactions,

thus securely immobilizing single atoms. Additionally, the specific characteristics of the support can strongly influence the electronic states of SACs, further impacting the catalytic performance of the CO_2RR. The majority of SACs used for the CO_2RR are carbon-based due to their excellent conductivity. Metals, metal oxides, and other supports with unique structural properties and coordination environments can offer more possibilities for tuning the performance of SACs.

We are well aware that copper is the only metal that exhibits appreciable activity towards the multi-electron transfer hydrocarbon products. In particular, Cu SACs exhibited distinct performance compared to non-Cu-based SACs in the generation of products such as methane, ethylene, acetone, etc.[82] However, Cu SACs usually undergo reconstruction involving atomic re-arrangement and compositional change during the CO_2RR process, and this uncontrollable electrochemical reconstruction not only leads to the inherently poor stability of Cu-based SACs, but also makes the investigation of real active sites and the establishment of structure-performance relationships shrouded in fog. Traditional carbon-based supports have shown some limitations in stabilizing atomically dispersed metal Cu.[165] Therefore, there is an urgent need to develop novel supports that can stabilize copper-based SACs to advance the field of CO_2RRs. Recently, inspired by traditional Cu/SiO$_2$ heterogeneous catalysts, Tan et al. have developed a method to stabilize atomic Cu by constructing a Cu–O–Si interface (Fig. 9a).[166] The as-prepared $CuSiO_x$ catalyst achieved an efficient electrochemical CO_2 methanation with a high faradaic efficiency of CH_4 (72.5% at −1.27 V vs. RHE) and excellent stability. To address the issue of poor conductivity of the oxide-based support, the authors also assembled a flow-cell device and achieved a remarkable CO_2-to-CH_4 conversion rate of 0.22 μmol cm^{-2} s^{-1}. More importantly, in situ X-ray absorption spectrum experiments indicated that the atomic Cu–O–Si interfacial sites exhibited ultra-high electrochemical stability and reconstruction-resistance over a broad potential window or long-time potentiostatic electrolysis, which attribute to the strong interactions between Cu and silica (Fig. 9b). Using CeO$_2$ as a support to enhance the stability of Cu is also a feasible approach. Zhou et al. reported a CeO$_x$-stabilized Cu^{2+} strategy (Cu–CeO$_x$) in which CeO$_2$ acts as a self-sacrificing component to protect the atomic Cu^{2+} active species.[167] They found that after CO_2RRs, the concentration of Ce^{3+} in Cu–CeO$_x$ increased significantly, as evidenced by in situ Raman spectroscopy experiments, indicating that electrons preferentially reduce Ce^{4+} to Ce^{3+} in Cu–CeO$_x$. Meanwhile, the newly formed Ce^{3+}/Ce^{4+} couple acts as a conductive network to enhance the conductivity of the overall solid solution. It can accelerate electron transfer and suppress the accumulation of electrons at Cu^{2+} sites, preventing them from self-reduction.

Oxygen vacancies or Lewis acid sites on metal oxides can also be utilized to modulate the activity of SACs. For instance, Wang et al. found that a single Cu atom substituted on the CeO$_2$(110) surface could stably enrich three oxygen vacancies around each Cu site, leading to an efficient CO_2 adsorption and activation center that promotes methane production.[106]
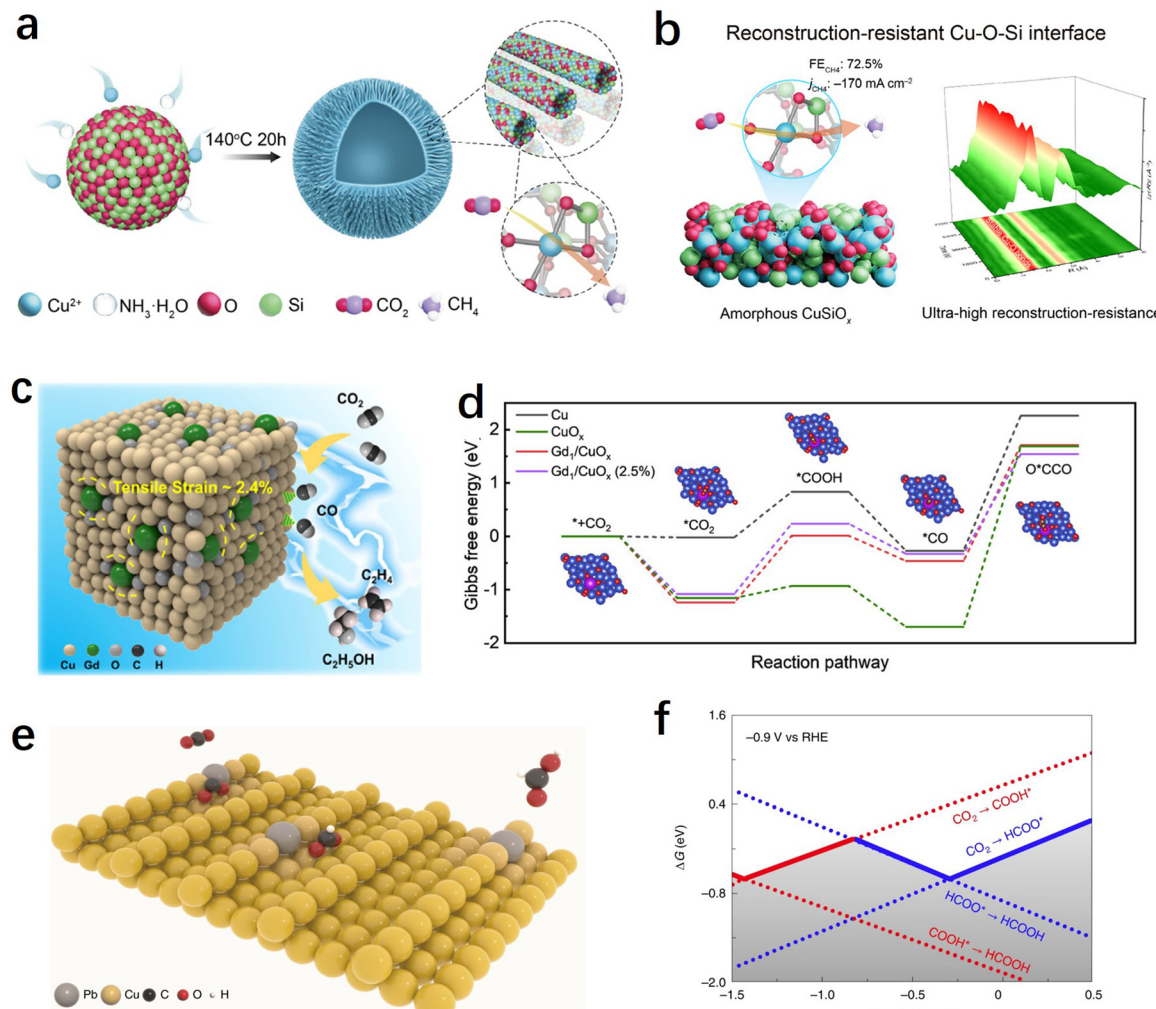
Fig. 9 (a) Schematic illustration of the CuSiO$_x$ synthetic process.[166] (b) The table of contents for the CuSiO$_x$ catalyst during the CO$_2$RR (including the schematic illustration and characterization of the reconstruction-resistance, and the CO$_2$RR performance).[166] (c) Illustration of C$_{2+}$ product generation promoted by stress engineering in Gd/CuO$_x$.[171] (d) Gibbs free energy diagrams of CO$_2$ reduction to O*CCO on surfaces of Cu, CuO$_x$, Gd$_1$/CuO$_x$, and Gd$_1$/CuO$_x$.[171] (e) Schematic illustration of CO$_2$ conversion into HCOOH over Pb$_1$Cu single-atom alloys.[38] (f) One-dimensional RPD for the CO$_2$RR. The solid lines show the G$_{RPD}$-limiting steps for the more favoured COOH* path and the HCOO* path.[38]

Chen et al. have demonstrated through theoretical predictions that the Lewis acid sites in metal oxides such as Al$_2$O$_3$ and Cr$_2$O$_3$ not only facilitate the activation of CO$_2$ but also lower the energy barrier for the *CH$_4$O intermediate, providing a favourable pathway for methane production.[168] Based on these findings, the authors synthesized Cu SACs supported on ultrathin Al$_2$O$_3$ nanosheets with strong Lewis acid sites. The catalyst exhibited an excellent electrochemical CO$_2$–CH$_4$ conversion performance, with a methane faradaic efficiency of 62% at −1.2 V vs. RHE. Yin et al. demonstrated that strong binding sites for CO$_2$ adsorption can be formed at the Cu–CeO$_2$ interface, promoting CO$_2$ activation and conversion into *CO intermediates on the nearby Cu surface.[169] As the Cu loading increases, the CO$_2$ reduction product can be tailored from C$_1$ to C$_{2+}$.

Using Cu-based materials as supports (such as metallic copper or copper oxides) and introducing atomically dispersed

heteroatoms into Cu is a highly effective approach for modulating the activity of Cu-based catalysts. Previous researches have indicated that Cu$^+$ sites played a crucial role in improving the selectivity of C$_{2+}$ products.[170] It can not only enhance the CO adsorption and facilitate C–C coupling reactions but also stabilize C$_2$ intermediates. However, Cu$^+$ was found to be unstable under negative potentials during the CO$_2$RR process. Feng et al. synthesized Gd-doped CuO$_x$ catalyst (Gd$_1$/CuO$_x$) using a simple one-step solvent thermal method.[171] The research findings demonstrated that atomically dispersed Gd can stabilize Cu$^+$ and induce tensile strain in the catalyst. The prepared Gd$_1$/CuO$_x$ exhibited excellent performance in CO$_2$-to-C$_{2+}$ product conversion, achieving a faradaic efficiency of 81.4% for C$_{2+}$ products at −0.8 V. Experimental and computational results suggested that Gd doping improved the stability of the crucial intermediate O*CCO, reduced the energy barrier for C–C coupling, and resulted in high CO$_2$RR-to-C$_{2+}$ product

performance (Fig. 9c and d). Zheng *et al.* synthesized a Pb-alloyed Cu catalyst, denoted as Pb_1Cu, by incorporating Pb single atoms onto the surface of metallic copper (Fig. 9e).[38] The introduction of Pb had a significant impact on the protonation process during the CO_2RR. Rather than occurring on the oxygen site, the initial protonation was observed to preferentially take place on the carbon site of CO_2 when Pb was present. This led to the formation of the *HCOO pathway instead of the *COOH pathway, resulting in Pb_1Cu demonstrating exceptional formate activity with an ultra-high faradaic efficiency of approximately 96% at current densities exceeding 1 A cm^{-2} (Fig. 9f). Moreover, the researchers utilized the Pb_1Cu catalyst to construct a solid electrolyte reactor, enabling the continuous production of pure formic acid solution for a remarkable duration of 180 hours, while maintaining a high current density above 100 mA cm^{-2}. These findings highlight the potential of Pb_1Cu as a promising catalyst for the CO_2RR and its application in the efficient and sustained production of formic acid.

In conclusion, adjusting the type, composition, and structure of the supports can optimize the electronic and geometric properties of SACs, enhancing the catalytic activity and stability. This holds significant importance for the efficient, stable, and sustainable development of SACs for the CO_2RR.

5. Conclusions and perspectives

The unique geometric/electronic structures of SACs qualify them as a new family of catalytic materials and a new frontier in the research field of CO_2RRs. In this review, we introduced the research status of SACs and summarized the synthesis strategies for SACs. Furthermore, we briefly introduced the fundamental parameters in the CO_2RR and attempted to summarize the possible reaction mechanisms for generating C_1 and C_2 products in the CO_2RR. Most importantly, we focused on discussing the structure–function relationship between the structure of SACs and the performance of CO_2RR, mainly manifested in the following four aspects of regulation: coordination environment regulation, diatomic sites regulation, tandem catalytic regulation, and catalyst support regulation. Although significant progress has been made in the synthesis of SACs as well as in the application of SACs in the CO_2RR and the establishment of their structure–function relationships, there are still certain limitations or challenges to the practical application of SACs in CO_2RRs. Summarized below are some potential research directions and challenges for SACs in CO_2RR applications in the future (Fig. 10).

1. Precise synthesis and characterization of SACs

The precise synthesis of SACs has always been a challenge for their application in various fields, including the CO_2RR. Metal single atoms are often fixed by the coordination of heteroatoms on the support owing to their high surface free energy. At present, the preparation of SACs often resorts to high-temperature calcination steps, which may lead to a certain degree of randomness in the generation of SACs. Many studies
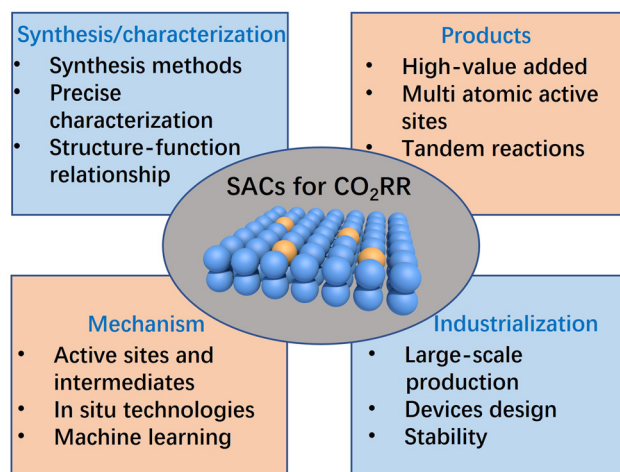

Fig. 10 Schematic illustration of future directions and challenges of SACs for the CO_2RR.

have shown that minor alterations in calcination temperature can lead to major changes in the coordination environment of SACs, and needless to say, their catalytic activity also changes accordingly. Therefore, when a high-temperature calcination step is used to prepare SACs, strict control of calcination conditions is necessary to ensure the repeatability of the preparation of different batches of catalysts. Obviously, a more precise strategy for preparing SACs has always been pursued, especially for the preparation of high-loading SACs, which currently faces greater difficulties. In addition, as the research on SACs in different applications deepens, there is increasing interest on multi-site catalysts (such as DACs). However, research on DACs is currently still in its early stages, and many basic concepts and standards have yet to be established. For instance, the characterization of SACs mainly depends on AC-HAADF-STEM and XAS technologies. AC-HAADF-STEM records the projected images of metal single atoms under the incident electron beam, and cannot distinguish the spatial arrangement of metal single atoms in close proximity; on the other hand, XAS records the average signal of the test sample, and cannot separate the information of a single active site. The limitations of these characterization techniques are particularly prominent in the analysis of DACs. Especially in the AC-HAADF-STEM images of DACs, the spatial arrangement of adjacent metal atoms cannot be determined by simply reading the high-contrast bright spots in the projected image while ignoring their spatial relationship along the incident electron beam. In this regard, one of our recent works attempts to identify "true/false" DACs by using *in situ* rotation operation in AC-HAADF-STEM characterization.[172] Therefore, more precise synthesis strategies and more advanced characterization methods need to be further explored, as the precise synthesis and characterization of SACs are prerequisites for understanding their structure–function relationship.

2. Rational design of SACs for producing non-CO products

As summarized in this review, considerably satisfactory CO selectivity has been achieved from the CO_2RR over a number of SACs, such as Fe, Ni, Mn, and Ag, but it still poses a great

challenge for high-value-added products beyond CO. There are two main reasons for this: (1) on the one hand, a single metal active site has moderate binding strength to the intermediate of CO_2RR, especially *COOH and *CO. Thus, *CO has a moderate desorption energy barrier, which is beneficial for the production of CO. (2) On the other hand, the atomically dispersed metal active sites are isolated from each other, leading to the physical separation of the intermediates, thus blocking further C–C coupling. Owing to its complex reaction mechanism and diverse reaction pathways, it is rather difficult to precisely control the distribution of the reaction products in the CO_2RR. In order to expand the product range of the CO_2RR and to obtain high-value-added products, two promising strategies could be explored. One is to rationally design DACs with multiple reaction active sites, which can provide mutually related synergistic active sites. The interrelated multiple active sites could provide a heteroatomic interface for asymmetric C–C coupling, which is expected to yield specific multi-carbon (C_{2+}) products. Another effective strategy is to construct tandem catalytic systems. The general principle is to combine SACs with high CO selectivity with Cu-based catalysts to achieve continuous conversion of CO_2 to CO and further to multi-carbon products, thus achieving high C_{2+} Faraday efficiencies. This method can promote the transfer of reaction intermediates and electrons, thereby improving reaction efficiency and selectivity. In addition, the tandem catalytic system lessens the difficulties in the catalyst design, and makes the catalytic reaction more controllable and predictable.

3. Deciphering the catalytic mechanisms of CO_2RRs

At present, significant progress has been made in both the synthesis of SACs and their application in CO_2RRs. However, owing to the diverse reaction pathways and complex reaction intermediates, the dynamic process and reaction mechanism of the CO_2RR are still difficult to understand. The catalytic activity of the CO_2RR is highly dependent on its active sites; therefore, the structure of the active site and its dynamic evolution during the catalytic reaction process are crucial. However, conventional characterization methods often detect the state of catalysts or catalytic reactions at a certain point in time but cannot monitor their dynamic evolution process. Therefore, it would be very helpful to use *in situ* technologies to identify the dynamic evolution of active sites and capture catalytic reaction intermediates, but this also requires more stringent test conditions. Currently, *in situ* tests are often conducted separately, such as *in situ* XAS, *in situ* TEM, and *in situ* Raman. It is expected that more advanced coupled *in situ* test techniques could be developed in the future to facilitate in-depth exploration of reaction mechanisms. In addition, machine learning has made significant progress in the preparation of nano-materials and its application in the CO_2RR, and it is expected to be introduced into the construction and performance prediction of SACs in the future. Machine learning can achieve high-throughput material performance prediction and assist in analyzing catalytic mechanisms, thus greatly reducing the trial-and-error costs.

4. Industrial-level applications

The industrial application of SACs in the CO_2RR is mainly focused on two aspects: large-scale synthesis of SACs and industrial-level performance of SACs in the CO_2RR. At present, a number of methods have been developed in the laboratory for the preparation of SACs, but a significant proportion of these methods are rather complex and cumbersome. The complex or harsh preparation conditions would result in poor repeatability of SACs preparation, thereby limiting its large-scale production. Moreover, apart from considerations regarding its repeatability, large-scale production of SACs also needs to balance economic benefits, which drives the preparation of SACs towards simpler, more efficient, and more reliable directions. On the other hand, in addition to achieving industrial-level preparation, SACs also need to meet industrial-level test conditions and performance indicators. As we already know, the low solubility of CO_2 in aqueous electrolytes greatly constrains its mass transport at high current densities, which is also a bottleneck for the industrialization of the CO_2RR. To address these issues, it has been attempted to combine SACs with gas diffusion layers and the assembly of membrane electrode components in flow cells, which helps to meet the requirements of industrial-level reactions and has made some notable progress thus far. However, reactors often fail during operation owing to various problems such as catalyst aggregation and membrane flooding, and these issues still need to be addressed one by one in future device design. In addition, the stability of SACs is also one of the evaluation metrics for their potentials of industrialization. Currently, the research on SACs in the CO_2RR is mainly focused on catalytic activity and selectivity, while stability tests often fail to meet the industrial requirements. Therefore, it is necessary to strengthen the research on catalyst stability in the future, to explore the deactivation mechanism of catalysts, and to design efficient SACs that feature balanced activity, selectivity, and stability.

Conflicts of interest

There are no conflicts to declare.

Acknowledgements

Notes and references

1 S. Chu, Y. Cui and N. Liu, *Nat. Mater.*, 2016, **16**, 16–22.
2 S. Gao, Y. Lin, X. Jiao, Y. Sun, Q. Luo, W. Zhang, D. Li, J. Yang and Y. Xie, *Nature*, 2016, **529**, 68–71.
3 S. Chu and A. Majumdar, *Nature*, 2012, **488**, 294–303.
4 D. R. Feldman, W. D. Collins, P. J. Gero, M. S. Torn, E. J. Mlawer and T. R. Shippert, *Nature*, 2015, **519**, 339–343.

5 H.-Y. Kuang, Y.-X. Lin, X.-H. Li and J.-S. Chen, *J. Mater. Chem. A*, 2021, **9**, 20857–20873.

6 A. Seiff and D. B. Kirk, *J. Geophys. Res.*, 1977, **82**, 4364–4378.

7 V. G. Dovì, F. Friedler, D. Huisingh and J. J. Klemeš, *J. Cleaner Prod.*, 2009, **17**, 889–895.

8 Z. Yuan, M. R. Eden and R. Gani, *Ind. Eng. Chem. Res.*, 2015, **55**, 3383–3419.

9 E. S. Sanz-Perez, C. R. Murdock, S. A. Didas and C. W. Jones, *Chem. Rev.*, 2016, **116**, 11840–11876.

10 H. Herring, *Energy*, 2006, **31**, 10–20.

11 C. Costentin, M. Robert and J.-M. Savéant, *Chem. Soc. Rev.*, 2013, **42**, 2423–2436.

12 E. V. Kondratenko, G. Mul, J. Baltrusaitis, G. O. Larrazábal and J. Pérez-Ramírez, *Energy Environ. Sci.*, 2013, **6**, 3112–3135.

13 J. Qiao, Y. Liu, F. Hong and J. Zhang, *Chem. Soc. Rev.*, 2014, **43**, 631–675.

14 M. Bevilacqua, J. Filippi, H. A. Miller and F. Vizza, *Energy Technol.*, 2015, **3**, 197–210.

15 Y. Li, S. H. Chan and Q. Sun, *Nanoscale*, 2015, **7**, 8663–8683.

16 W. H. Wang, Y. Himeda, J. T. Muckerman, G. F. Manbeck and E. Fujita, *Chem. Rev.*, 2015, **115**, 12936–12973.

17 M. Li, H. Wang, W. Luo, P. C. Sherrell, J. Chen and J. Yang, *Adv. Mater.*, 2020, **32**, e2001848.

18 H. Gu, J. Wu and L. Zhang, *Nano Res.*, 2022, **15**, 9747–9763.

19 T. N. Nguyen, M. Salehi, Q. V. Le, A. Seifitokaldani and C. T. Dinh, *ACS Catal.*, 2020, **10**, 10068–10095.

20 X. Tan, Z. Zhuang, Y. Zhang, K. Sun and C. Chen, *Chem. Commun.*, 2023, **59**, 2682–2696.

21 S. Wang, L. Wang, D. Wang and Y. Li, *Energy Environ. Sci.*, 2023, **16**, 2759–2803.

22 M. Schreier, F. Héroguel, L. Steier, S. Ahmad, J. S. Luterbacher, M. T. Mayer, J. Luo and M. Grätzel, *Nat. Energy*, 2017, **2**, 17087.

23 K. Li, B. Peng and T. Peng, *ACS Catal.*, 2016, **6**, 7485–7527.

24 Y. Wang, Y. Liu, W. Liu, J. Wu, Q. Li, Q. Feng, Z. Chen, X. Xiong, D. Wang and Y. Lei, *Energy Environ. Sci.*, 2020, **13**, 4609–4624.

25 S. G. Han, D. D. Ma and Q. L. Zhu, *Small Methods*, 2021, **5**, e2100102.

26 Y. Wang, P. Han, X. Lv, L. Zhang and G. Zheng, *Joule*, 2018, **2**, 2551–2582.

27 Y. Cheng, S. Yang, S. P. Jiang and S. Wang, *Small Methods*, 2019, **3**, 1800440.

28 C. Cao, D. D. Ma, J. Jia, Q. Xu, X. T. Wu and Q. L. Zhu, *Adv. Mater.*, 2021, **33**, e2008631.

29 C. J. Peng, G. Zeng, D. D. Ma, C. Cao, S. Zhou, X. T. Wu and Q. L. Zhu, *ACS Appl. Mater. Interfaces*, 2021, **13**, 20589–20597.

30 Y. Zhao, X. Tan, W. Yang, C. Jia, X. Chen, W. Ren, S. C. Smith and C. Zhao, *Angew. Chem., Int. Ed.*, 2020, **59**, 21493–21498.

31 R. M. Arán-Ais, F. Scholten, S. Kunze, R. Rizo and B. Roldan Cuenya, *Nat. Energy*, 2020, **5**, 317–325.

32 D. Zhong, Z. J. Zhao, Q. Zhao, D. Cheng, B. Liu, G. Zhang, W. Deng, H. Dong, L. Zhang, J. Li, J. Li and J. Gong, *Angew. Chem., Int. Ed.*, 2021, **60**, 4879–4885.

33 W. Zhang, Q. Qin, L. Dai, R. Qin, X. Zhao, X. Chen, D. Ou, J. Chen, T. T. Chuong, B. Wu and N. Zheng, *Angew. Chem., Int. Ed.*, 2018, **57**, 9475–9479.

34 A. Eilert, F. S. Roberts, D. Friebel and A. Nilsson, *J. Phys. Chem. Lett.*, 2016, **7**, 1466–1470.

35 L.-P. Yuan, W.-J. Jiang, X.-L. Liu, Y.-H. He, C. He, T. Tang, J. Zhang and J.-S. Hu, *ACS Catal.*, 2020, **10**, 13227–13235.

36 Z. Chen, M.-R. Gao, N. Duan, J. Zhang, Y.-Q. Zhang, T. Fan, J. Zhang, Y. Dong, J. Li, Q. Liu, X. Yi and J.-L. Luo, *Appl. Catal., B*, 2020, **277**, 119252.

37 T. Yuan, Z. Hu, Y. Zhao, J. Fang, J. Lv, Q. Zhang, Z. Zhuang, L. Gu and S. Hu, *Nano Lett.*, 2020, **20**, 2916–2922.

38 T. Zheng, C. Liu, C. Guo, M. Zhang, X. Li, Q. Jiang, W. Xue, H. Li, A. Li, C. W. Pao, J. Xiao, C. Xia and J. Zeng, *Nat. Nanotechnol.*, 2021, **16**, 1386–1393.

39 H. Xie, Y. Wan, X. Wang, J. Liang, G. Lu, T. Wang, G. Chai, N. M. Adli, C. Priest, Y. Huang, G. Wu and Q. Li, *Appl. Catal., B*, 2021, **289**, 119783.

40 T. Shen, S. Wang, T. Zhao, Y. Hu and D. Wang, *Adv. Energy Mater.*, 2022, **12**, 2201823.

41 R. T. Hannagan, G. Giannakakis, M. Flytzani-Stephanopoulos and E. C. H. Sykes, *Chem. Rev.*, 2020, **120**, 12044–12088.

42 M. E. Ahmed, S. Adam, D. Saha, J. Fize, V. Artero, A. Dey and C. Duboc, *ACS Energy Lett.*, 2020, **5**, 3837–3842.

43 J. Xu, S. Lai, M. Hu, S. Ge, R. Xie, F. Li, D. Hua, H. Xu, H. Zhou, R. Wu, J. Fu, Y. Qiu, J. He, C. Li, H. Liu, Y. Liu, J. Sun, X. Liu and J. Luo, *Small Methods*, 2020, **4**, 2000567.

44 Z. Chen, X. Zhang, M. Jiao, K. Mou, X. Zhang and L. Liu, *Adv. Energy Mater.*, 2020, **10**, 1903664.

45 X. Ma, J. Du, H. Sun, F. Ye, X. Wang, P. Xu, C. Hu, L. Zhang and D. Liu, *Appl. Catal., B*, 2021, **298**, 120543.

46 A. Vasileff, Y. Zheng and S. Z. Qiao, *Adv. Energy Mater.*, 2017, **7**, 1700759.

47 C. Chen, X. Sun, X. Yan, Y. Wu, H. Liu, Q. Zhu, B. B. A. Bediako and B. Han, *Angew. Chem., Int. Ed.*, 2020, **59**, 11123–11129.

48 W. Zhu and C. Chen, *Chem*, 2019, **5**, 2737–2739.

49 A. Wang, J. Li and T. Zhang, *Nat. Rev. Chem.*, 2018, **2**, 65–81.

50 X. Liang, N. Fu, S. Yao, Z. Li and Y. Li, *J. Am. Chem. Soc.*, 2022, **144**, 18155–18174.

51 B. Qiao, A. Wang, X. Yang, L. F. Allard, Z. Jiang, Y. Cui, J. Liu, J. Li and T. Zhang, *Nat. Chem.*, 2011, **3**, 634–641.

52 S. Zhang, X. Ao, J. Huang, B. Wei, Y. Zhai, D. Zhai, W. Deng, C. Su, D. Wang and Y. Li, *Nano Lett.*, 2021, **21**, 9691–9698.

53 N. Fu, X. Liang, Z. Li, W. Chen, Y. Wang, L. Zheng, Q. Zhang, C. Chen, D. Wang, Q. Peng, L. Gu and Y. Li, *Nano Res.*, 2020, **13**, 947–951.

54 J. Zhang, Y. Zhao, X. Guo, C. Chen, C.-L. Dong, R.-S. Liu, C.-P. Han, Y. Li, Y. Gogotsi and G. Wang, *Nat. Catal.*, 2018, **1**, 985–992.

55 Q. Li, Z. Li, Q. Zhang, L. Zheng, W. Yan, X. Liang, L. Gu, C. Chen, D. Wang, Q. Peng and Y. Li, *Nano Res.*, 2020, **14**, 1435–1442.

56 J. Yang, W. H. Li, S. Tan, K. Xu, Y. Wang, D. Wang and Y. Li, *Angew. Chem., Int. Ed.*, 2021, **60**, 19085–19091.

57 Y. Chen, S. Ji, C. Chen, Q. Peng, D. Wang and Y. Li, *Joule*, 2018, **2**, 1242–1264.

58 S. Ji, Y. Chen, X. Wang, Z. Zhang, D. Wang and Y. Li, *Chem. Rev.*, 2020, **120**, 11900–11955.

59 S. Meshitsuka, M. Ichikawa and K. Tamaru, *J. Chem. Soc., Chem. Commun.*, 1974, 158–159.

60 Z. Sun, T. Ma, H. Tao, Q. Fan and B. Han, *Chem*, 2017, **3**, 560–587.

61 R. Li and D. Wang, *Adv. Energy Mater.*, 2022, **12**, 2103564.

62 H. Liu, H. Rong and J. Zhang, *ChemSusChem*, 2022, **15**, e202200498.

63 Q. An, J. Jiang, W. Cheng, H. Su, Y. Jiang and Q. Liu, *Small Methods*, 2022, **6**, e2200408.

64 Y. Ying, X. Luo, J. Qiao and H. Huang, *Adv. Funct. Mater.*, 2020, **31**, 2007423.

65 Y. Hu, Z. Li, B. Li and C. Yu, *Small*, 2022, **18**, e2203589.

66 Y. N. Gong, C. Y. Cao, W. J. Shi, J. H. Zhang, J. H. Deng, T. B. Lu and D. C. Zhong, *Angew. Chem., Int. Ed.*, 2022, **61**, e202215187.

67 W. Zhang, Y. Chao, W. Zhang, J. Zhou, F. Lv, K. Wang, F. Lin, H. Luo, J. Li, M. Tong, E. Wang and S. Guo, *Adv. Mater.*, 2021, **33**, e2102576.

68 F. Pan and Y. Yang, *Energy Environ. Sci.*, 2020, **13**, 2275–2309.

69 H. Rabiee, L. Ge, X. Zhang, S. Hu, M. Li and Z. Yuan, *Energy Environ. Sci.*, 2021, **14**, 1959–2008.

70 R. Kortlever, J. Shen, K. J. Schouten, F. Calle-Vallejo and M. T. Koper, *J. Phys. Chem. Lett.*, 2015, **6**, 4073–4082.

71 J. Rosen, G. S. Hutchings, Q. Lu, S. Rivera, Y. Zhou, D. G. Vlachos and F. Jiao, *ACS Catal.*, 2015, **5**, 4293–4299.

72 W. Ju, A. Bagger, G. P. Hao, A. S. Varela, I. Sinev, V. Bon, B. Roldan Cuenya, S. Kaskel, J. Rossmeisl and P. Strasser, *Nat. Commun.*, 2017, **8**, 944.

73 T. K. Todorova, M. W. Schreiber and M. Fontecave, *ACS Catal.*, 2019, **10**, 1754–1768.

74 S. Vijay, W. Ju, S. Brückner, S.-C. Tsang, P. Strasser and K. Chan, *Nat. Catal.*, 2021, **4**, 1024–1031.

75 A. A. Peterson, F. Abild-Pedersen, F. Studt, J. Rossmeisl and J. K. Nørskov, *Energy Environ. Sci.*, 2010, **3**, 1311–1315.

76 X. Nie, M. R. Esopi, M. J. Janik and A. Asthagiri, *Angew. Chem., Int. Ed.*, 2013, **52**, 2459–2462.

77 Z. Pan, K. Wang, K. Ye, Y. Wang, H.-Y. Su, B. Hu, J. Xiao, T. Yu, Y. Wang and S. Song, *ACS Catal.*, 2020, **10**, 3871–3880.

78 G. Wang, J. Chen, Y. Ding, P. Cai, L. Yi, Y. Li, C. Tu, Y. Hou, Z. Wen and L. Dai, *Chem. Soc. Rev.*, 2021, **50**, 4993–5061.

79 H. Mistry, A. S. Varela, C. S. Bonifacio, I. Zegkinoglou, I. Sinev, Y. W. Choi, K. Kisslinger, E. A. Stach, J. C. Yang, P. Strasser and B. R. Cuenya, *Nat. Commun.*, 2016, **7**, 12123.

80 T. T. H. Hoang, S. Ma, J. I. Gold, P. J. A. Kenis and A. A. Gewirth, *ACS Catal.*, 2017, **7**, 3313–3321.

81 B. Zhang, B. Zhang, Y. Jiang, T. Ma, H. Pan and W. Sun, *Small*, 2021, **17**, e2101443.

82 K. Zhao, X. Nie, H. Wang, S. Chen, X. Quan, H. Yu, W. Choi, G. Zhang, B. Kim and J. G. Chen, *Nat. Commun.*, 2020, **11**, 2455.

83 D. Karapinar, N. T. Huan, N. Ranjbar Sahraie, J. Li, D. Wakerley, N. Touati, S. Zanna, D. Taverna, L. H. Galvão Tizei, A. Zitolo, F. Jaouen, V. Mougel and M. Fontecave, *Angew. Chem., Int. Ed.*, 2019, **131**, 15242–15247.

84 P. Shao, W. Zhou, Q. L. Hong, L. Yi, L. Zheng, W. Wang, H. X. Zhang, H. Zhang and J. Zhang, *Angew. Chem., Int. Ed.*, 2021, **60**, 16687–16692.

85 Q. Liu, J. Ma and C. Chen, *Chin. J. Catal.*, 2022, **43**, 898–912.

86 X. Wang, Z. Chen, X. Zhao, T. Yao, W. Chen, R. You, C. Zhao, G. Wu, J. Wang, W. Huang, J. Yang, X. Hong, S. Wei, Y. Wu and Y. Li, *Angew. Chem., Int. Ed.*, 2018, **57**, 1944–1948.

87 Y. Zhang, L. Jiao, W. Yang, C. Xie and H. L. Jiang, *Angew. Chem., Int. Ed.*, 2021, **60**, 7607–7611.

88 Y. Hou, Y.-L. Liang, P.-C. Shi, Y.-B. Huang and R. Cao, *Appl. Catal., B*, 2020, **271**, 118929.

89 L. Jiao, J. Zhu, Y. Zhang, W. Yang, S. Zhou, A. Li, C. Xie, X. Zheng, W. Zhou, S. H. Yu and H. L. Jiang, *J. Am. Chem. Soc.*, 2021, **143**, 19417–19424.

90 Q. Cao, L.-L. Zhang, C. Zhou, J.-H. He, A. Marcomini and J.-M. Lu, *Appl. Catal., B*, 2021, **294**, 120238.

91 Y. Zhou, L. Chen, L. Sheng, Q. Luo, W. Zhang and J. Yang, *Nano Res.*, 2022, **15**, 7994–8000.

92 Y. Zhu, X. Yang, C. Peng, C. Priest, Y. Mei and G. Wu, *Small*, 2021, **17**, e2005148.

93 S. Chen, W. H. Li, W. Jiang, J. Yang, J. Zhu, L. Wang, H. Ou, Z. Zhuang, M. Chen, X. Sun, D. Wang and Y. Li, *Angew. Chem., Int. Ed.*, 2022, **61**, e202114450.

94 Y. S. Wei, M. Zhang, R. Zou and Q. Xu, *Chem. Rev.*, 2020, **120**, 12089–12174.

95 S. Mallakpour, F. Sirous and C. M. Hussain, *Top. Curr. Chem.*, 2021, **380**, 7.

96 Q. Hao, H.-x Zhong, J.-z Wang, K.-h Liu, J.-m Yan, Z.-h Ren, N. Zhou, X. Zhao, H. Zhang, D.-x Liu, X. Liu, L.-w Chen, J. Luo and X.-b Zhang, *Nat. Synth.*, 2022, **1**, 719–728.

97 J. Fonseca, T. Gong, L. Jiao and H.-L. Jiang, *J. Mater. Chem. A*, 2021, **9**, 10562–10611.

98 Y. Yun, H. Zeng, L. Li, H. Li, S. Cheng, N. Sun, M. Li, H. Sheng, S. Hu, T. Yao and M. Zhu, *Adv. Mater.*, 2023, **35**, e2209561.

99 B. Xu, H. Wang, W. Wang, L. Gao, S. Li, X. Pan, H. Wang, H. Yang, X. Meng, Q. Wu, L. Zheng, S. Chen, X. Shi, K. Fan, X. Yan and H. Liu, *Angew. Chem., Int. Ed.*, 2019, **131**, 4965–4970.

100 Z. Li, Y. Chen, S. Ji, Y. Tang, W. Chen, A. Li, J. Zhao, Y. Xiong, Y. Wu, Y. Gong, T. Yao, W. Liu, L. Zheng, J. Dong, Y. Wang, Z. Zhuang, W. Xing, C. T. He, C. Peng, W. C. Cheong, Q. Li, M. Zhang, Z. Chen, N. Fu, X. Gao, W. Zhu, J. Wan, J. Zhang, L. Gu, S. Wei, P. Hu, J. Luo, J. Li, C. Chen, Q. Peng, X. Duan, Y. Huang, X. M. Chen, D. Wang and Y. Li, *Nat. Chem.*, 2020, **12**, 764–772.

101 C. Zhao, X. Dai, T. Yao, W. Chen, X. Wang, J. Wang, J. Yang, S. Wei, Y. Wu and Y. Li, *J. Am. Chem. Soc.*, 2017, **139**, 8078–8081.

102 X. Jiang, H. Li, J. Xiao, D. Gao, R. Si, F. Yang, Y. Li, G. Wang and X. Bao, *Nano Energy*, 2018, **52**, 345–350.

103 Z. Li, D. He, X. Yan, S. Dai, S. Younan, Z. Ke, X. Pan, X. Xiao, H. Wu and J. Gu, *Angew. Chem., Int. Ed.*, 2020, **132**, 18731–18736.

104 N. Mohd Adli, W. Shan, S. Hwang, W. Samarakoon, S. Karakalos, Y. Li, D. A. Cullen, D. Su, Z. Feng, G. Wang and G. Wu, *Angew. Chem., Int. Ed.*, 2020, **133**, 1035–1045.

105 G. Hai, X. Xue, S. Feng, Y. Ma and X. Huang, *ACS Catal.*, 2022, **12**, 15271–15281.

106 Y. Wang, Z. Chen, P. Han, Y. Du, Z. Gu, X. Xu and G. Zheng, *ACS Catal.*, 2018, **8**, 7113–7119.

107 C. Jia, S. Li, Y. Zhao, R. K. Hocking, W. Ren, X. Chen, Z. Su, W. Yang, Y. Wang, S. Zheng, F. Pan and C. Zhao, *Adv. Funct. Mater.*, 2021, **31**, 2107072.

108 X. Zu, X. Li, W. Liu, Y. Sun, J. Xu, T. Yao, W. Yan, S. Gao, C. Wang, S. Wei and Y. Xie, *Adv. Mater.*, 2019, **31**, e1808135.

109 H. Zou, G. Zhao, H. Dai, H. Dong, W. Luo, L. Wang, Z. Lu, Y. Luo, G. Zhang and L. Duan, *Angew. Chem., Int. Ed.*, 2023, **62**, e202217220.

110 G. Shi, Y. Xie, L. Du, X. Fu, X. Chen, W. Xie, T. B. Lu, M. Yuan and M. Wang, *Angew. Chem., Int. Ed.*, 2022, **61**, e202203569.

111 J. Jiao, R. Lin, S. Liu, W. C. Cheong, C. Zhang, Z. Chen, Y. Pan, J. Tang, K. Wu, S. F. Hung, H. M. Chen, L. Zheng, Q. Lu, X. Yang, B. Xu, H. Xiao, J. Li, D. Wang, Q. Peng, C. Chen and Y. Li, *Nat. Chem.*, 2019, **11**, 222–228.

112 Z. Ma, T. Wan, D. Zhang, J. A. Yuwono, C. Tsounis, J. Jiang, Y. H. Chou, X. Lu, P. V. Kumar, Y. H. Ng, D. Chu, C. Y. Toe, Z. Han and R. Amal, *ACS Nano*, 2023, **17**, 2387–2398.

113 M. B. Ross, C. T. Dinh, Y. Li, D. Kim, P. De Luna, E. H. Sargent and P. Yang, *J. Am. Chem. Soc.*, 2017, **139**, 9359–9363.

114 N. Xuan, J. Chen, J. Shi, Y. Yue, P. Zhuang, K. Ba, Y. Sun, J. Shen, Y. Liu, B. Ge and Z. Sun, *Chem. Mater.*, 2018, **31**, 429–435.

115 Z. Wang, J. Yang, J. Cao, W. Chen, G. Wang, F. Liao, X. Zhou, F. Zhou, R. Li, Z. Q. Yu, G. Zhang, X. Duan and Y. Wu, *ACS Nano*, 2020, **14**, 6164–6172.

116 Y. Qu, Z. Li, W. Chen, Y. Lin, T. Yuan, Z. Yang, C. Zhao, J. Wang, C. Zhao, X. Wang, F. Zhou, Z. Zhuang, Y. Wu and Y. Li, *Nat. Catal.*, 2018, **1**, 781–786.

117 Z. Yang, B. Chen, W. Chen, Y. Qu, F. Zhou, C. Zhao, Q. Xu, Q. Zhang, X. Duan and Y. Wu, *Nat. Commun.*, 2019, **10**, 3734.

118 B. Wang, X. Zhu, X. Pei, W. Liu, Y. Leng, X. Yu, C. Wang, L. Hu, Q. Su, C. Wu, Y. Yao, Z. Lin and Z. Zou, *J. Am. Chem. Soc.*, 2023, **145**, 13788–13795.

119 J. Yang, Z. Qiu, C. Zhao, W. Wei, W. Chen, Z. Li, Y. Qu, J. Dong, J. Luo, Z. Li and Y. Wu, *Angew. Chem., Int. Ed.*, 2018, **57**, 14095–14100.

120 E. Zhang, T. Wang, K. Yu, J. Liu, W. Chen, A. Li, H. Rong, R. Lin, S. Ji, X. Zheng, Y. Wang, L. Zheng, C. Chen, D. Wang, J. Zhang and Y. Li, *J. Am. Chem. Soc.*, 2019, **141**, 16569–16573.

121 S. Wei, A. Li, J. C. Liu, Z. Li, W. Chen, Y. Gong, Q. Zhang, W. C. Cheong, Y. Wang, L. Zheng, H. Xiao, C. Chen, D. Wang, Q. Peng, L. Gu, X. Han, J. Li and Y. Li, *Nat. Nanotechnol.*, 2018, **13**, 856–861.

122 C. Zhao, Y. Wang, Z. Li, W. Chen, Q. Xu, D. He, D. Xi, Q. Zhang, T. Yuan, Y. Qu, J. Yang, F. Zhou, Z. Yang, X. Wang, J. Wang, J. Luo, Y. Li, H. Duan, Y. Wu and Y. Li, *Joule*, 2019, **3**, 584–594.

123 Y. Qu, L. Wang, Z. Li, P. Li, Q. Zhang, Y. Lin, F. Zhou, H. Wang, Z. Yang, Y. Hu, M. Zhu, X. Zhao, X. Han, C. Wang, Q. Xu, L. Gu, J. Luo, L. Zheng and Y. Wu, *Adv. Mater.*, 2019, **31**, e1904496.

124 H. Yang, Q. Lin, Y. Wu, G. Li, Q. Hu, X. Chai, X. Ren, Q. Zhang, J. Liu and C. He, *Nano Energy*, 2020, **70**, 104454.

125 C. Xia, Y. Qiu, Y. Xia, P. Zhu, G. King, X. Zhang, Z. Wu, J. Y. T. Kim, D. A. Cullen, D. Zheng, P. Li, M. Shakouri, E. Heredia, P. Cui, H. N. Alshareef, Y. Hu and H. Wang, *Nat. Chem.*, 2021, **13**, 887–894.

126 H. Chung, D. Cullen, D. Higgins, B. Sneed, E. Holby, K. More and P. Zelenay, *Science*, 2017, **357**, 479–484.

127 Y. Li, C. Chen, R. Cao, Z. Pan, H. He and K. Zhou, *Appl. Catal., B*, 2020, **268**, 118747.

128 U. Kramm, L. Ni and S. Wagner, *Adv. Mater.*, 2019, **31**, 1805623.

129 Z. Jin, P. Li, Y. Meng, Z. Fang, D. Xiao and G. Yu, *Nat. Catal.*, 2021, **4**, 615–622.

130 R. Chen, J. Zhao, Y. Li, Y. Cui, Y. Lu, S. Hung, S. Wang, W. Wang, G. Huo, Y. Zhao, W. Liu, J. Wang, H. Xiao, X. Li, Y. Huang and B. Liu, *J. Am. Chem. Soc.*, 2023, **145**, 20683–20691.

131 K. Li, W. Wang, H. Zheng, X. Wang, Z. Xie, L. Ding, S. Yu, Y. Yao and F. Zhang, *Mater. Today Phys.*, 2021, **19**, 100427.

132 D. Zhao, K. Yu, P. Song, W. Feng, B. Hu, W.-C. Cheong, Z. Zhuang, S. Liu, K. Sun, J. Zhang and C. Chen, *Energy Environ. Sci.*, 2022, **15**, 3795–3804.

133 Z. Zhang, J. Zhu, S. Chen, W. Sun and D. Wang, *Angew. Chem., Int. Ed.*, 2023, **62**, e202215136.

134 H. Xiao, W. A. Goddard, 3rd, T. Cheng and Y. Liu, *Proc. Natl. Acad. Sci. U. S. A.*, 2017, **114**, 6685–6688.

135 C. Liu, Y. Wu, K. Sun, J. Fang, A. Huang, Y. Pan, W.-C. Cheong, Z. Zhuang, Z. Zhuang, Q. Yuan, H. L. Xin, C. Zhang, J. Zhang, H. Xiao, C. Chen and Y. Li, *Chem*, 2021, **7**, 1297–1307.

136 K. Sun, K. Yu, J. Fang, Z. Zhuang, X. Tan, Y. Wu, L. Zeng, Z. Zhuang, Y. Pan and C. Chen, *Adv. Mater.*, 2022, **34**, e2206478.

137 J. Masana, J. Xiao, H. Zhang, X. Lu, M. Qiu and Y. Yu, *Appl. Catal., B*, 2023, **323**, 122199.

138 Z. Chen, A. Huang, K. Yu, T. Cui, Z. Zhuang, S. Liu, J. Li, R. Tu, K. Sun, X. Tan, J. Zhang, D. Liu, Y. Zhang, P. Jiang, Y. Pan, C. Chen, Q. Peng and Y. Li, *Energy Environ. Sci.*, 2021, **14**, 3430–3437.

139 Y. Pan, R. Lin, Y. Chen, S. Liu, W. Zhu, X. Cao, W. Chen, K. Wu, W. C. Cheong, Y. Wang, L. Zheng, J. Luo, Y. Lin, Y. Liu, C. Liu, J. Li, Q. Lu, X. Chen, D. Wang, Q. Peng, C. Chen and Y. Li, *J. Am. Chem. Soc.*, 2018, **140**, 4218–4221.

140 J. R. Huang, X. F. Qiu, Z. H. Zhao, H. L. Zhu, Y. C. Liu, W. Shi, P. Q. Liao and X. M. Chen, *Angew. Chem., Int. Ed.*, 2022, **61**, e202210985.

141 J.-X. Peng, W. Yang, Z. Jia, L. Jiao and H.-L. Jiang, *Nano Res.*, 2022, **15**, 10063–10069.

142 C. Chen, Z. Chen, J. Zhong, X. Song, D. Chen, S. Liu, W. Cheong, J. Li, X. Tan, C. He, J. Zhang, D. Liu, Q. Yuan, C. Chen, Q. Peng and Y. Li, *Nano Res.*, 2023, **16**, 4211–4218.

143 X. Liu, Y. Liu, W. Yang, X. Feng and B. Wang, *Chemistry*, 2022, **28**, e202201471.

144 B. Huang, S. Huang, C. Lu, L. Li, J. Chen, T. Hu, D. Lützenkirchen-Hecht, K. Yuan, X. Zhuang and Y. Chen, *CCS Chem.*, 2022, 1–12, DOI: **10.31635/ccschem.022.202202241**.

145 N. Qiu, J. Li, H. Wang and Z. Zhang, *Sci. China Mater.*, 2022, **65**, 3302–3323.

146 S. Li, A. Guan, C. Yang, C. Peng, X. Lv, Y. Ji, Y. Quan, Q. Wang, L. Zhang and G. Zheng, *ACS Mater. Lett.*, 2021, **3**, 1729–1737.

147 W. Ren, X. Tan, W. Yang, C. Jia, S. Xu, K. Wang, S. C. Smith and C. Zhao, *Angew. Chem., Int. Ed.*, 2019, **58**, 6972–6976.

148 J. D. Yi, X. Gao, H. Zhou, W. Chen and Y. Wu, *Angew. Chem., Int. Ed.*, 2022, **61**, e202212329.

149 Y. Pan, C. Liu, N. Zhang, M. Li, M. Wang, X. Yang, H.-C. Chen, Y. Zhang, W. Hu, W. Yan, H. M. Chen, S. Liu, H. Xiao, J. Li and C. Chen, *Chem Catal.*, 2023, **3**, 100610.

150 Z. Liang, L. Song, M. Sun, B. Huang and Y. Du, *Nano Res.*, 2023, **16**, 8757–8764.

151 W. Zheng, X. Yang, Z. Li, B. Yang, Q. Zhang, L. Lei and Y. Hou, *Angew. Chem., Int. Ed.*, 2023, e202307283.

152 F. Li, Y. Li, Z. Wang, J. Li, D. Nam, Y. Lum, M. Luo, X. Wang, A. Ozden, S. Hung, B. Chen, Y. Wang, J. Wicks, Y. Xu, Y. Li, C. Gabardo, C. Dinh, Y. Wang, T. Zhuang, D. Sinton and E. Sargent, *Nat. Catal*, 2020, **3**, 75–82.

153 Y. Zhou, F. Che, M. Liu, C. Zou, Z. Liang, P. Luna, H. Yuan, J. Li, Z. Wang, H. Xie, H. Li, P. Chen, E. Bladt, R. Quintero, T. Sham, S. Bals, J. Hofkens, D. Sinton, G. Chen and E. Sargent, *Nat. Chem.*, 2018, **10**, 974–980.

154 Z. Yin, J. Yu, Z. Xie, S. W. Yu, L. Zhang, T. Akauola, J. G. Chen, W. Huang, L. Qi and S. Zhang, *J. Am. Chem. Soc.*, 2022, **144**, 20931–20938.

155 D. L. Meng, M. D. Zhang, D. H. Si, M. J. Mao, Y. Hou, Y. B. Huang and R. Cao, *Angew. Chem., Int. Ed.*, 2021, **60**, 25485–25492.

156 B. Cao, F.-Z. Li and J. Gu, *ACS Catal.*, 2022, **12**, 9735–9752.

157 M. Wang, A. Loiudice, V. Okatenko, I. D. Sharp and R. Buonsanti, *Chem. Sci.*, 2023, **14**, 1097–1104.

158 L. Lin, T. Liu, J. Xiao, H. Li, P. Wei, D. Gao, B. Nan, R. Si, G. Wang and X. Bao, *Angew. Chem., Int. Ed.*, 2020, **59**, 22408–22413.

159 H. Deng, C. Guo, P. Shi and G. Zhao, *ChemCatChem*, 2021, **13**, 4325–4333.

160 T. Zhang, B. Yuan, W. Wang, J. He and X. Xiang, *Angew. Chem., Int. Ed.*, 2023, **62**, e202302096.

161 J. Zhang, P. Yu, C. Peng, X. Lv, Z. Liu, T. Cheng and G. Zheng, *ACS Catal.*, 2023, **13**, 7170–7177.

162 S. Chen, Z. Zhang, W. Jiang, S. Zhang, J. Zhu, L. Wang, H. Ou, S. Zaman, L. Tan, P. Zhu, E. Zhang, P. Jiang, Y. Su, D. Wang and Y. Li, *J. Am. Chem. Soc.*, 2022, **144**, 12807–12815.

163 H. Xiao, T. Cheng and W. Goddard, *J. Am. Chem. Soc.*, 2017, **139**, 130–136.

164 T. Cheng, H. Xiao and W. Goddard, *J. Phys. Chem. Lett.*, 2015, **6**, 4767–4773.

165 D. Karapinar, N. T. Huan, N. Ranjbar Sahraie, J. Li, D. Wakerley, N. Touati, S. Zanna, D. Taverna, L. H. Galvao Tizei, A. Zitolo, F. Jaouen, V. Mougel and M. Fontecave, *Angew. Chem., Int. Ed.*, 2019, **58**, 15098–15103.

166 X. Tan, K. Sun, Z. Zhuang, B. Hu, Y. Zhang, Q. Liu, C. He, Z. Xu, C. Chen, H. Xiao and C. Chen, *J. Am. Chem. Soc.*, 2023, **145**, 8656–8664.

167 X. Zhou, J. Shan, L. Chen, B. Y. Xia, T. Ling, J. Duan, Y. Jiao, Y. Zheng and S. Z. Qiao, *J. Am. Chem. Soc.*, 2022, **144**, 2079–2084.

168 S. Chen, B. Wang, J. Zhu, L. Wang, H. Ou, Z. Zhang, X. Liang, L. Zheng, L. Zhou, Y. Q. Su, D. Wang and Y. Li, *Nano Lett.*, 2021, **21**, 7325–7331.

169 J. Yin, Z. Gao, F. Wei, C. Liu, J. Gong, J. Li, W. Li, L. Xiao, G. Wang, J. Lu and L. Zhuang, *ACS Catal.*, 2022, **12**, 1004–1011.

170 X. Yuan, S. Chen, D. Cheng, L. Li, W. Zhu, D. Zhong, Z. J. Zhao, J. Li, T. Wang and J. Gong, *Angew. Chem., Int. Ed.*, 2021, **60**, 15344–15347.

171 J. Feng, L. Wu, S. Liu, L. Xu, X. Song, L. Zhang, Q. Zhu, X. Kang, X. Sun and B. Han, *J. Am. Chem. Soc.*, 2023, **145**, 9857–9866.

172 C. Chen, Y. Li, A. Huang, X. Liu, J. Li, Y. Zhang, Z. Chen, Z. Zhuang, Y. Wu, W. Cheong, X. Tan, K. SUn, Z. Xu, D. Liu, Z. Wang, K. Zhou and C. Chen, *J. Am. Chem. Soc.*, 2023, **145**, 21273–21283.